J. Fluid Mech. (2000), *vol.* 422, *pp.* 281–317. Printed in the United Kingdom

Lubrication theory in highly compressible porous media: the mechanics of skiing, from red cells to humans

By J. FENG† AND S. WEINBAUM‡

Center for Biomedical Engineering and Department of Mechanical Engineering,
The City College of the City University of New York, New York, NY 10031, USA

(Received 15 November 1999 and in revised form 7 June 2000)

A generalized lubrication theory that is applicable to highly deformable porous layers is developed using an effective-medium approach (Brinkman equation). This theory is valid in the limit where the structure is so compressible that the normal forces generated by elastic compression of the fibres comprising the solid phase are negligible compared to the pressure forces generated within the porous layer. We assume that the deformation of the solid phase is primarily due to boundary compression as opposed to the motion of the fluid phase. A generalized Reynolds equation is derived in which the spatial variation of the Darcy permeability parameter, $\alpha = H/\sqrt{K_p}$, due to the matrix compression is determined by new local hydrodynamic solutions for the flow through a simplified periodic fibre model for the deformed matrix. Here H is the undeformed layer thickness and K_p the Darcy permeability. This simplified model assumes that the fibres compress linearly with the deformed gap height in the vertical direction, but the fibre spacing in the horizontal plane remains unchanged. The model is thus able to capture the essential nonlinearity that results from large-amplitude deformations of the matrix layer.

The new theory shows that there is an unexpected striking similarity between the gliding motion of a red cell moving over the endothelial glycocalyx that lines our microvessels and a human skier or snowboarder skiing on compressed powder. In both cases one observes an order-of-magnitude compression of the matrix layer when the motion is arrested and predicts values of α that are of order 100. In this large-α limit one finds that the pressure and lift forces generated within the compressed matrix are four orders-of-magnitude greater than classical lubrication theory. In the case of the red cell these repulsive forces may explain why red cells do not experience constant adhesive molecular interactions with the endothelial plasmalemma, whereas in the case of the skier or snowboarder the theory explains why a 70 kg human can glide through compressed powder without sinking to the base as would occur if the motion is arrested. The principal difference between the tightly fitting red cell and the snowboarder is the lateral leakage of the excess pressure at the edges of the snowboard which greatly diminishes the lift force. A simplified axisymmetric model is presented for the red cell to explain the striking pop out phenomenon in which a red cell that starts from rest will quickly lift off the surface and then glide near the edge of the glycocalyx and also for the unexpectedly large apparent viscosity measured by Pries *et al.* (1994) *in vivo*.

† Current address: CFD Research Corporation, 215 Wynn Drive, Huntsville, AL 35805, USA.
‡ To whom correspondence should be addressed: weinbaum@med2s0.engr.ccny.cuny.edu

1. Introduction

In this paper we shall present the detailed development of a generalized lubrication theory based on an effective-medium approach (Brinkman equation) that is applicable to highly deformable porous layers. In particular, we shall want to look into the limit where the porous structure is so compressible that the normal forces generated by elastic compression of the fibres comprising the solid phase are negligible compared with the pressure force generated within the porous layer and the deformation of the solid phase is primarily due to boundary compression as opposed to the motion of the fluid phase. The most important new feature that we wish to capture in the model is the large nonlinearity that results from order-of-magnitude spatial variations in Darcy permeability that arise from the large-amplitude deformations of the fibre matrix. We shall show that the lift forces generated in such layers can be orders of magnitude larger than the lift forces generated in classical lubrication theory. Existing lubrication analyses have been limited to either a pure fluid layer satisfying a classical Reynolds equation or mixture or biphasic theories where the matrix deformation is small enough to neglect the changes in Darcy permeability due to the compression. The generalized Reynolds equation derived herein reduces to the analysis in Damiano (1998) and Secomb *et al.* (1998) for the case of one-dimensional flow with uniform Darcy permeability.

The initial motivation for this study grew out of several fundamental questions relating to the role of the thin fibre matrix layers that surround cells in an *in vivo* fluid environment, see Weinbaum (1998). One of the most important of these layers is the endothelial glycocalyx, a negatively charged layer of glycoproteins and proteoglycans that uniformly coats the luminal surface of vascular endothelium. This layer has been estimated to vary from 0.1 μm in *in vitro* studies of frog mesentery capillaries, Adamson & Clough (1992), to 0.4 μm in *in vivo* studies of hamster cremaster microvessels, Vink & Duling (1996). From a hydrodynamic viewpoint this layer can be thought of as a hydrated gel, whose fibre volume fraction has been theoretically estimated to be between 1 and 2%, (Curry 1986; Weinbaum, Tsay & Curry 1992). This extracellular layer has recently been proposed to be the primary molecular filter or osmotic barrier that determines the Starling forces that act across vascular endothelium (Michel 1997; Weinbaum 1998; Hu & Weinbaum 1999). To serve this function the barrier must exclude albumin (7 nm in diameter) and other plasma proteins. Since numerous permeability studies in many tissues have shown that the reflection coefficient approaches 1.0 as the solute size approaches that of albumin, the open gap between fibres has generally been assumed to be close to 7 nm, at least in the sieving part of the layer. This hypothesis is strongly supported by the recent experiments described in Henry & Duling (1999) where it is shown that low molecular weight dextrans of comparable size to albumin do not penetrate the glycocalyx *in vivo* unless its permeability is altered by an enzyme that is known to degrade the hyaluronan side chains of the matrix.

While the existence of the surface glycocalyx has been known for several decades, Luft (1965), it is only in the past few years that its importance in capillary hemodynamics and cell motion has been appreciated (Vink & Duling 1996; Damiano 1998; Secomb, Hsu & Pries 1998). In the case of the mammalian red cell, 8 μm diameter cells are easily able to squeeze through 5–6 μm true capillaries with a separation distance near the wall that is typically 0.5 to 0.6 μm when the cells are moving at typical speeds of several hundred microns per second, Vink & Duling (1996). However, this separation distance appears to essentially vanish when the motion of the red cells is arrested, indicating that the matrix layer is highly deformable and more flexible

than the membrane cytoskeleton of the red cell. In larger microvessels, where the red cells may not travel in single file, a similar separation distance is observed (Henry & Duling 1999; Schmid-Schoenbein 1999). One of the most puzzling conundrums is the large difference in the *in vitro* and *in vivo* viscosity laws measured when the resistance of red cells in capillary networks is compared with their motion in small glass tubes (Pries, Neuhaus & Gaehtgens 1992; Pries *et al.* 1994). Significant differences start to appear for vessels smaller than 40 μm diameter, which grow to an order of magnitude or more for true capillaries. In the case of white cells the tips of the microvilli are known to be coated with adhesion molecules that promote the tethering and adhesive interaction of leukocytes with transmembrane receptors and ligands in the endothelial plasmalemma. The interaction of these microvilli with the endothelial glycocalyx is treated for the first time in Feng, Ganatos & Weinbaum (1998).

While these fundamental biological questions provided the initial motivation for the new theory proposed herein, the critical insights for understanding these phenomena arose from crude measurements by the senior author of the depth of ski tracks in freshly fallen snow at a ski resort in the northern Catskills. Nearly every experienced skier will tell you that skiing on dry powder is like riding on air. Expert skiers achieve velocities in excess of ten times their body height per second due to gravitational forcing. However, this relative velocity is small compared to that which the red cell experiences in navigating through the microcirculation due to pressure forcing. A red cell can achieve a velocity that approaches 100 times its diameter per second. The fact that a red cell can travel at such velocities in microvessels less than their diameter and survive on average for 120 days without undergoing hemolysis is one of the miracles of microcirculatory mechanics. Both dry snow powder and the endothelial glycocalyx share a common property that they are highly porous and easily compressed. Neither will support the compressive forces they are subjected to when the motion of the red cell or skier is arrested. Snow will compress tenfold when it has to bear the static load due to the weight of the skier and, as noted above, a red cell will crush the surface glycocalyx and fill nearly the entire lumen of a microvessel due to the elastic restoring forces in its membrane and cytoskeleton when its motion is arrested. The crude measurement of the depth of the ski tracks readily confirmed that the skier could rise off the packed base and create a thin layer of partially compressed dry powder beneath the ski. Rough estimates of the lift forces predicted using a conventional lubrication theory based on a classical Reynolds equation indicate that such forces would support a weight of order 10 g for a constrained air layer beneath the ski at small tilt angles. This is four orders of magnitude smaller than the weight of a 70 kg human being with his/her skis. The Darcy permeability, K_p, of snow has been measured for various conditions, Jordan *et al.* (1999), but there are no data to our knowledge which show the variation of K_p with compression. We shall use a fibre matrix model which predicts values for K_p which compare favourably with measured values for fresh snow powder and then assume that this powder compresses in a manner that is similar to the endothelial glycocalyx.

The foregoing observation suggested that there might be a striking similarity between a human skier or snowboarder gliding through dry snow powder and the red cell skimming along the surface of the endothelial glycocalyx. In the case of snow the lift forces generated by the porous media protect the bottom of our skis from the roughness of the surface beneath the powder and in the case of the red cell the endothelial surface glycocalyx prevents molecular-level adhesive interactions between the endothelial surface and the red cell membrane. This membrane can be thought of as a snowboard and the red cell itself as an extraordinarily efficient skier. In both

cases, we shall show that the pressure forces generated within the compressed porous layer are approximately four orders of magnitude greater than predicted by classical lubrication theory where the gap is filled with a pure fluid. However, the red cell is far more efficient since for the human skier or snowboarder much of the excess pressure that is built up beneath the planing surface leaks out at the lateral edges of the ski or snowboard.

1.1. *Previous models for red cell motion*

Numerous models based on classical lubrication theory have been developed over the years to describe the motion of red cells in microvessels. Until 1995 the vessel wall was treated as a circular cylindrical tube without matrix. The red cells were initially modelled as either rigid or deformable pellets (Lighthill 1968; Barnard, Lopez & Hellums 1969) or periodic arrays of spheres (Wang & Skalak 1969; Tozeren & Skalak 1978). More sophisticated models were then developed to predict the axisymmetric deformed shape of a moving cell using measured properties of the red cell membrane (Secomb & Gross 1983; Secomb *et al.* 1986). In the latter studies membrane shearing and bending stresses are treated within the framework of axisymmetric lubrication theory. It is only recently that the critical role of the endothelial surface glycocalyx in red cell motion has been recognized. The so-called 'sugar coat' of glycoprotein fibres was first identified by Luft (1965), but it was not until 1992 that Adamson & Clough (1992) clearly demonstrated *in vitro* that this coat was of nearly uniform thickness (0.1 μm) and that this thickness depends on the proteins present in the perfusate. The first *in vivo* measurement of the glycocalyx in hamster cremaster microvessels by Vink & Duling (1996) indicated a significantly thicker glycocalyx (0.4 μm) than the electromicroscopic studies of Adamson & Clough, where the thickness could have been underestimated due to dehydration artifacts. Vink & Duling also demonstrated that if the glycocalyx were non-invasively removed using epifluorescence, the red cell would fill the entire lumen. Perhaps most intriguing, if a red cell were started from rest it would exhibit a striking pop out phenomenon in which it would quickly lift off the surface and then glide near the outer edge of the matrix layer.

The first models that attempted to take account of the matrix layer, Damiano *et al.* (1995) and Wang & Parker (1995), used lubrication and binary mixture theory to describe the motion of rigid particles in a circular tube whose walls were covered by a porous medium. In more recent analyses, Damiano (1998) and Secomb *et al.* (1998) have extended this model to a deformable cell without bending stiffness which moves within the fluid core. Damiano assumes that a thin pure fluid layer exists between the edge of the glycocalyx and the red cell membrane, whereas Secomb *et al.* assume a value for K_p that varies with distance from the wall and vanishes in the fluid core. This model allows for the penetration of the matrix but not its compression. The presence of a matrix free fluid layer between the red cell and the glycocalyx provides a low-resistance pathway for the relaxation of the pressure in the matrix and the new phenomena described in this paper are absent. No previous model has attempted to describe the penetration of the red cell into a compressible matrix or the pop out phenomenon wherein the cell rises off the wall at low velocity. Furthermore, the zero drag condition, which describes the global force balance on the red cell, must be modified to take account of the integrated distributed force of the fibres.

1.2. *Skiing, snowboarding and tobogganing*

To our knowledge this is the first time that the mechanics of skiing or snowboarding has been approached from the viewpoint presented in this paper. The theory in its

present form is most applicable to a snowboard or toboggan moving on a layer of dry compressed powder, since the lateral dimensions of a typical ski, 10 cm, are too narrow for lubrication theory approximations to be rigorously applied. Nevertheless, if the present results are integrated across the width of the ski they provide a centreline theory for a long, slender planing surface. There is an extensive literature on the hydrodynamics of water skiing or planing on a free surface. The fundamental lift mechanism in the latter application is inertial and not viscous and the lift forces are generated by the momentum of the fluid that is pushed ahead of the planing surface. This mechanism might be operative in snow ploughing or turning, where the edges of the skis or snowboard are turned into the snow, but it is intuitively clear that large lift forces cannot be generated by the inertia of the snow in the normal skiing position because of the low angle of attack relative to the snow surface and the fact that the density of the snow is only about a tenth that of water. On the other hand, the viscous lift forces predicted by classical lubrication theory, as noted previously, would be several orders of magnitude too small. In the new theory two mechanisms contribute to the tremendous increase in the lift force and the pressure distribution under the planing surface. One is the large increase in the resistance of the air due to the fact that it is literally pushed and dragged through the porous solid. The resulting velocity profiles and streamlines depart dramatically from those in classical lubrication theory. The second is the compression of the soft powder which greatly increases the fluid resistance and the lift force acting at the back of the planing surface. By slightly adjusting the angle of tilt the skier or snowboarder can regulate the centre of pressure and come to an equilibrium position where moments due to gravity and pressure cancel each other. In skiing, snowboarding or tobogganing the snow will compress and the permeability parameter α will increase until the lift force is just sufficient to balance the gravitational force.

The fundamental difference between the red cell gliding on the endothelial glycocalyx and skiing or snowboarding is the pressure relaxation that occurs at the lateral edges of the planing surface. This pressure loss is characterized by a second parameter that appears in the governing equation, namely the aspect ratio L/W of the ski or snowboard. For the same value of α, the dimensionless lift forces will be at least two orders of magnitude lower than for the red cell. This is compensated for by a greater density of the matrix. For the endothelial glycocalyx the estimated volume fraction of the glycosaminoglycan (GAG) side chains in the undeformed solid phase is approximately 1% to 2% and is unlikely to increase much beyond 10% during compression. This is an order of magnitude smaller than the fibres that form the crystals in a snow flake.

1.3. *Deformation of the porous media*

In mixture theory, which has been applied to the artery wall (Kenyon 1979) or articular cartilage (Lai & Mow 1980; Hou *et al.* 1991), there is a governing equation for the solid phase which relates the deformation of the porous matrix to the fluid flow. In the present approach we shall propose a much simplified model for the elastic deformation of the solid matrix phase based on the fact that this deformation is assumed to occur primarily due to the normal compressive force between the confining boundaries and not the fluid force on the matrix elements. This is a good approximation for the endothelial glycocalyx since experiments have shown that the matrix is not disrupted even by the passage of a tightly fitting white cell and that the glycocalyx rebounds in less than a second to its initial thickness due to weak osmotic forces that are associated with the trapping of proteins by matrix fibres (Vink &

Duling 1996). The same behaviour is observed in the red cell pop out phenomenon where the glycocalyx quickly rebounds after the red cell motion starts (Vink, private communication). In the case of snow the solid phase moves due to the pressure gradient established by the motion of the air, but this velocity is small compared to that of the air that passes through the porous medium both because of packing and the large difference in the density of the two phases. It is thus a reasonable assumption to neglect the motion of the crystal phase and assume that the air is passing through a porous structure that deforms without flowing. In contrast to the glycocalyx, snow crystals have little or no rebound. However, this difference is inconsequential since the osmotic restoring forces in the glycocalyx are small compared to the lifting forces generated by the motion of the red cell over the compressed matrix.

The simplified model that we have constructed for the fibrous network lining the vasculature assumes that the side chains of the glycoproteins form a two-dimensional, diamond-shaped, parallel array perpendicular to the flow direction. The matrix compresses linearly with gap height in the normal direction, but in planes parallel to the lower boundary the fibre spacing remains unchanged since there is negligible compression in the lateral direction. However, the normal compression can induce a large increase in the hydrodynamic resistance in the direction of flow. It is this increase in fluid resistance due to the matrix that produces the large increase in pressure in the fibre layer. In this simplified model, the Darcy permeability is a function of just two dimensionless geometric parameters: the aspect ratio of the periodic fibre array and the ratio of the initial undeformed fibre spacing and the fibre radius. The local hydrodynamic resistance, or Darcy permeability, is then calculated using creeping flow theory. This simple model retains the essential physics of the compression process, and is a reasonable approximation to the much more complicated three-dimensional fibre structure of the surface glycocalyx about which little is at present known. For snow, no attempt is made to model the hexagonal crystal structure of the snow flake. The model is intended only as a guide in predicting the variation of K_p with change in snow layer thickness due to compression. The model predictions for skiing or snowboarding should be reasonable since they provide reasonable agreement with the measured value of K_p for snow in the undeformed state.

The paper is organized into seven sections. In § 2, a new Reynolds-type equation is derived for highly compressible porous media in which the Darcy permeability is spatially varying. In § 3 we develop the theory for predicting the spatial variation of the local Darcy permeability. In § 4 we simplify the governing equation for a one-dimensional planar surface where we assume there is no lateral leakage of pressure. The resulting highly nonlinear differential equation is solved for large deformations to show the effects of varying both the slope of the moving boundary and the permeability parameter α. Results are shown for the pressure distribution, lift force, velocity profiles and the streamline pattern. In § 5 we generalize these results for two-dimensional planar surfaces with lateral edges as a model for skiing and snowboarding. In § 6 we first derive a new global force balance for the zero drag condition on the cell and then examine the pressure drop and apparent viscosity for axisymmetric rigid models of red cells to provide new insight into the *in vivo* viscosity law of Pries *et al.* (1994). Concluding comments and future directions are given in § 7.

2. Lubrication theory for the porous layer

Classical lubrication theory was initially developed by Reynolds for incompressible, Newtonian fluid (Schlichting 1954). This was subsequently generalized for Newtonian

fluids with variable properties and non-Newtonian fluids. The theory has been applied to both impermeable and porous stationary and moving journal-bearing systems. In biological applications, where the stresses are associated with the compression of a porous solid phase, biphasic mixture theory has been extensively used to described cartilage, Lai & Mow (1980), and more recently the endothelial glycocalyx (Wang & Parker 1995; Damiano 1998; Secomb *et al.* 1998). In most of these previous analyses the deformation of the porous matrix is sufficiently small for the Darcy permeability to remain constant. As a result, the velocity profile in the lubricating layer depends only on the local value of the pressure gradient and boundary velocity. However, as the porous layer, which in the present application is either the endothelial surface glycocalyx or dry snow powder, is compressed by the planing surface, the change of the Darcy permeability K_p can be huge. This can lead to dramatic changes in the pressure distribution in the matrix for large compressions. In the present theory, a simplified anisotropic fibre matrix model is developed to account for the local variation of the matrix permeability. Consequently, an additional parameter, which depends on the local matrix height, appears in the new Reynolds-type equation derived using effective-medium theory. For two-dimensional lubricating layer theory, which is required for studying the mechanics of skiing or snowboarding, the geometric aspect ratio of the planing surface will also play an important role.

For the general case, we consider a two-dimensional rigid boundary moving arbitrarily with velocity $\boldsymbol{U} = (U_x, U_x, U_z)$ in Cartesian coordinates over a fibre layer which is thin compared to the characteristic dimensions of the moving boundary in the x- and y-directions. The local matrix height is denoted by $h(x, y)$. Note that $\boldsymbol{U}$ and h cannot be specified independently, because there is a simple Eulerian relationship between them:

$$U_z = \frac{\partial h}{\partial t} + U_x \frac{\partial h}{\partial x} + U_y \frac{\partial h}{\partial y}. \tag{2.1}$$

Nevertheless, it it convenient to treat $\boldsymbol{U}$ and h as though they were independent.

The effective-medium theory for flow in a fibre layer is described by the Brinkman equation (Brinkman 1947)

$$\mu \left(\nabla^2 - \frac{1}{K_p} \right) \boldsymbol{u} = \nabla p. \tag{2.2}$$

The important difference between the present application of equation (2.2) and previous studies is that a rational theoretical framework is formulated for predicting the local spatial variation of K_p for large-amplitude compressions. Equation (2.2) can be derived either by renormalization of the Stokes flow equation in a periodic microscopic domain or by averaging the Stokes equation for flow in a random assemblage of spherical particles (Howells 1974; Tam 1969; Lundgren 1972). Recently, Howells (1998) studied flow through randomly distributed fibres by a renormalization technique and recovered the Brinkman equation at the leading order. Feng *et al.* (1998) have developed a boundary integral equation method for bounded particle motion in a Brinkman medium and have applied the results to several biological problems in cellular mechanics and transendothelial transport. The validity and accuracy of the Brinkman equation in bounded porous media is also addressed in Tsay & Weinbaum (1991) and Feng *et al.* (1998).

While it is obvious that inertial effects can be neglected in (2.2) for the endothelial glycocalyx, this is not true for skiing or snowboarding. If inertial forces were added in the x momentum equation this term would be $O(\rho U_x^2/L)$. In contrast, the Darcy term is $O(\mu U_x/K_p)$. Thus, the Darcy term would be greater than the inertial term provided

$U_x < \mu L/\rho K_p$. Since K_p for the undeformed matrix can also be written as $K_p = H^2/\alpha^2$, where H is the thickness of the undeformed porous medium, this constraint on U_x can also be written as $U_x < \nu L\alpha^2/H^2$ where $\nu = \mu/\rho$ is the kinematic viscosity. Our results in § 5 show that α will typically vary between 100 and 400. Thus, for a representative compressed powder layer where $L = 1.5\,\text{m}$, $H = 5\,\text{cm}$ and $\nu = 0.1\,\text{cm}^2\,\text{s}^{-1}$ at 0°C, the upper bound for U_x will fall in the range 60 to $960\,\text{m}\,\text{s}^{-1}$. A similar analysis could be applied in the y-direction and one would require $U_y < \nu W\alpha^2/H^2$ where W is the width of the snowboard. A typical snowboard has an aspect ratio of 5 and, thus, if $W = 30\,\text{cm}$, $U_y < 12\,\text{m}\,\text{s}^{-1}$ for $\alpha = 100$ and $< 192\,\text{m}\,\text{s}^{-1}$ for $\alpha = 400$. The actual magnitude of the characteristic air velocity generated beneath the snowboard is readily estimated by examining the characteristic pressure gradient developed in the x- and y-directions beneath the snowboard. The characteristic pressure P_c due to the weight of the snowboarder is $P_c = Mg/LW$. The characteristic pressure gradient Mg/L^2W generated by the Darcy resistance, $\mu U_x/K_p$, in the x-direction, therefore, leads to a characteristic value for U_x of order $MgH^2/\mu L^2W\alpha^2$. For a 70 kg human U_x is approximately $20\,\text{m}\,\text{s}^{-1}$ for $\alpha = 100$ and $1.2\,\text{m}\,\text{s}^{-1}$ for $\alpha = 400$. These values for U_x are significantly smaller than the value for U_x where inertial forces are significant except for values of α at the very low end. In general, one finds that there is a characteristic minimum value of α where inertia should be considered. This minimum value of α is given by

$$\alpha = \frac{H}{L}\left[\frac{\rho Mg}{\mu^2}\left(\frac{L}{W}\right)\right]^{1/4}. \tag{2.3}$$

We introduce the dimensionless primed coordinates, velocities and pressure as

$$x' = \frac{x}{L}, \quad y' = \frac{y}{W}, \quad z' = \frac{z}{H}, \tag{2.4}$$

$$u' = \frac{u}{U_c}, \quad v' = \frac{v}{V_c}, \quad w' = \frac{w}{W_c}, \quad p' = \frac{p}{P_c}, \tag{2.5}$$

where L and W are the characteristic lengths of the moving surface in the x- and y-directions. For a ski or a snowboard, L and W are its length and width, respectively. H is the undeformed matrix gap height. In these dimensionless variables, the continuity equation in Cartesian coordinates is rewritten as

$$\frac{\partial u'}{\partial x'} + \frac{V_c}{U_c}\frac{L}{W}\frac{\partial v'}{\partial y'} + \frac{W_c}{U_c}\frac{L}{H}\frac{\partial w'}{\partial z'} = 0. \tag{2.6}$$

For the coefficient of the dimensionless pressure gradient in the x-, y- and z-directions to be unity, we choose the characteristic velocities as

$$U_c = U_x, \quad V_c = \frac{L}{W}U_x, \quad W_c = \frac{H}{L}U_x, \tag{2.7}$$

and define the characteristic pressure P_c as

$$P_c = \frac{\mu L U_x}{H^2}. \tag{2.8}$$

With these definitions of the characteristic velocities and pressure, the three components of the Brinkman equation in (2.2) in Cartesian coordinates can be written as

$$\frac{\partial p'}{\partial x'} = \left(\epsilon_x^2\frac{\partial^2}{\partial x'^2} + \epsilon_y^2\frac{\partial^2}{\partial y'^2} + \frac{\partial^2}{\partial z'^2} - \alpha^2\right)u', \tag{2.9}$$

$$\frac{\partial p'}{\partial y'} = \left(\epsilon_x^2 \frac{\partial^2}{\partial x'^2} + \epsilon_y^2 \frac{\partial^2}{\partial y'^2} + \frac{\partial^2}{\partial z'^2} - \alpha^2\right) v', \tag{2.10}$$

$$\frac{\partial p'}{\partial z'} = \epsilon_x^2 \left(\epsilon_x^2 \frac{\partial^2}{\partial x'^2} + \epsilon_y^2 \frac{\partial^2}{\partial y'^2} + \frac{\partial^2}{\partial z'^2} - \alpha^2\right) w', \tag{2.11}$$

where $\epsilon_x = H/L$, $\epsilon_y = H/W$ and α is a dimensionless permeability parameter defined in terms of K_p the Darcy permeability parameter,

$$\alpha = \frac{H}{\sqrt{K_p}}. \tag{2.12}$$

If we assume that both $\epsilon_x \ll O(1)$ and $\epsilon_y \ll O(1)$, then it is clearly seen from (2.9)–(2.11) that the pressure gradient in the vertical direction is $O(\epsilon_x^2)$ smaller than that in either lateral direction. Thus we assume that the pressure is a constant across the matrix layer, i.e. $p = p(x, y)$, and to $O(\epsilon_x^2)$ or $O(\epsilon_y^2)$ equations (2.9) and (2.10) reduce to equations similar to those obtained in classical lubrication theory (prime omitted for brevity)

$$\frac{\partial p}{\partial x} = \left(\frac{\partial^2}{\partial z^2} - \alpha^2\right) u, \tag{2.13}$$

$$\frac{\partial p}{\partial y} = \left(\frac{\partial^2}{\partial z^2} - \alpha^2\right) v. \tag{2.14}$$

These equations in conjunction with the dimensionless continuity equation

$$\frac{\partial u}{\partial x} + \frac{L^2}{W^2}\frac{\partial v}{\partial y} + \frac{\partial w}{\partial z} = 0 \tag{2.15}$$

determine the flow within the thin layer of fibre matrix.

Solutions to (2.13) and (2.14) which satisfy the no-slip boundary conditions at $z = 0$ and $z = h$, the local dimensionless channel height, are given by

$$u = \frac{\sinh \alpha z}{\sinh \alpha h} + \frac{1}{\alpha^2}\frac{\partial p}{\partial x}\left[\cosh \alpha z - 1 - \frac{\sinh \alpha z}{\sinh \alpha h}(\cosh \alpha h - 1)\right] \tag{2.16}$$

$$v = \frac{W}{L}\frac{U_y}{U_x}\frac{\sinh \alpha z}{\sinh \alpha h} + \frac{1}{\alpha^2}\frac{\partial p}{\partial y}\left[\cosh \alpha z - 1 - \frac{\sinh \alpha z}{\sinh \alpha h}(\cosh \alpha h - 1)\right]. \tag{2.17}$$

Note that in view of the definition of V_c in (2.7), v at $z = h$ is given by $(W/L)(U_y/U_x)$. The corresponding fluxes in the x- and y-directions are computed by integrating over the local dimensionless channel height, i.e.

$$Q_x = \int_0^h u \, dz = f(\alpha, h) + \frac{1}{\alpha^2}\frac{\partial p}{\partial x}(2f(\alpha, h) - h), \tag{2.18}$$

$$Q_y = \int_0^h v \, dz = \frac{W}{L}\frac{U_y}{U_x} f(\alpha, h) + \frac{1}{\alpha^2}\frac{\partial p}{\partial y}(2f(\alpha, h) - h), \tag{2.19}$$

in which

$$f = \frac{\cosh \alpha h - 1}{\alpha \sinh \alpha h}. \tag{2.20}$$

If we integrate the continuity equation (2.6) over the channel height and satisfy the

dimensionless boundary conditions

$$U'_x(x,y,h)=1, \quad U'_y(x,y,h)=\frac{W}{L}\frac{U_y}{U_x}, \quad U'_z(x,y,h)=\frac{L}{H}\frac{U_z}{U_x}, \tag{2.21}$$

we obtain

$$\frac{\partial Q_x}{\partial x}+\frac{L^2}{W^2}\frac{\partial Q_y}{\partial y}=-\frac{U_z}{\epsilon_x U_X}+\frac{\partial h}{\partial x}+\frac{L}{W}\frac{U_y}{U_x}\frac{\partial h}{\partial y}, \tag{2.22}$$

where the prime has been dropped for convenience. Inserting (2.18) and (2.19) in (2.22), one obtains a generalized Reynolds equation for a Brinkman medium

$$\frac{\partial}{\partial x}\left[f+\frac{1}{\alpha^2}\frac{\partial p}{\partial x}(2f-h)\right]+\frac{L^2}{W^2}\frac{\partial}{\partial y}\left[\frac{W}{L}\frac{U_y}{U_x}f+\frac{1}{\alpha^2}\frac{\partial p}{\partial y}(2f-h)\right]=\frac{\partial h}{\partial x}+\frac{L}{W}\frac{U_y}{U_x}\frac{\partial h}{\partial y}-\frac{1}{\epsilon_x}\frac{U_z}{U_x}. \tag{2.23}$$

In the limit $\alpha \to 0$,

$$f \to \frac{h}{2}-\frac{\alpha^2 h^3}{24},$$

and equation (2.23) reduces to the classical Reynolds equation for an incompressible, Newtonian viscous fluid,

$$\frac{\partial}{\partial x}\left[6h-h^3\frac{\partial p}{\partial x}\right]+\frac{L^2}{W^2}\frac{\partial}{\partial y}\left[6\frac{W}{L}\frac{U_y}{U_x}h-h^3\frac{\partial p}{\partial y}\right]=12\left[\frac{\partial h}{\partial x}+\frac{L}{W}\frac{U_y}{U_x}\frac{\partial h}{\partial y}-\frac{1}{\epsilon_x}\frac{U_z}{U_x}\right] \tag{2.24}$$

The lateral velocity components are given by (2.16) and (2.17). The vertical velocity component w is calculated from the dimensionless continuity equation (2.15).

In the case of one-dimensional flow, where $\boldsymbol{U}=u_x\boldsymbol{i}$ and there is no flow leakage in the y-direction, equation (2.23) reduces to

$$\frac{\mathrm{d}}{\mathrm{d}x}\left[f+\frac{1}{\alpha^2}\frac{\mathrm{d}p}{\mathrm{d}x}(2f-h)\right]=\frac{\mathrm{d}h}{\mathrm{d}x}. \tag{2.25}$$

This one-dimensional equation is suitable for describing the gliding motion of a red cell membrane over the endothelial glycocalyx. Equation (2.25) is nonlinear since K_p and hence α is a nonlinear function of x if large compressions of the matrix are considered. K_p is determined from the solution of equations (3.2) and (3.3), presented in the next section.

The modified Reynolds equation (2.23) can be solved for the pressure distribution using the appropriate boundary conditions. Once the pressure field is determined, the flow field, the lift force and the drag exerted on the moving membrane can be calculated. These results, together with new features, which are absent for a pure fluid layer, are discussed in subsequent sections.

3. Permeability of the porous layer

In this section, we propose a simplified model for the local change in Darcy permeability that is suitable for both the endothelial glycocalyx and the flexible crystals comprising snow powder. A schematic illustration of the geometry of the model for the sliding motion of a planar membrane over a thin fibre matrix layer is shown in figure 1(*a*). For simplicity, we model this surface matrix as a doubly periodic fibre array with lateral and vertical fibre spacings Δ_1 and Δ_2, see figure 1(*c*, *d*). The Darcy permeability K_p of the matrix depends upon the fibre radius a and the spacing, which varies with position as a result of the non-uniform compression.

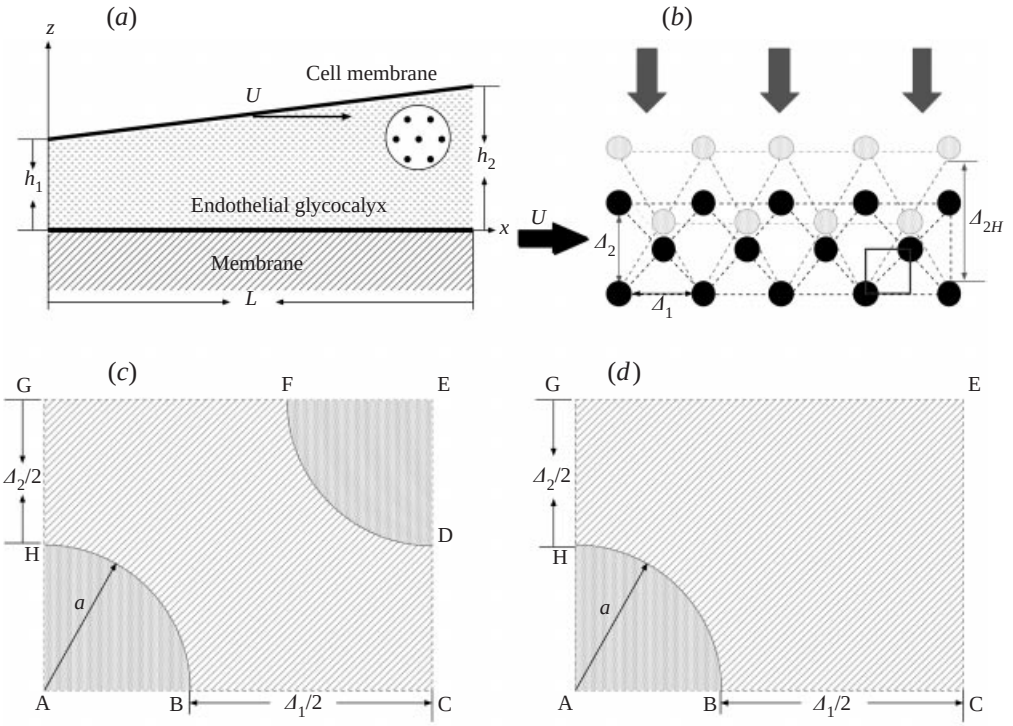

FIGURE 1. (*a*) Schematic illustration of the present model for sliding motion of a rigid surface over a thin layer of fibre matrix. (*b*) Blow-up of the inset in (*a*) shows an idealized model for the fibre matrix which is composed of doubly periodic array of cylindrical fibres of radius a. The undeformed fibre spacings in the lateral and vertical directions are denoted by Δ_1 and Δ_{2H}, respectively. (*c*) A unit cell for a deformed hexagonal fibre array in which the Stokes equation is solved for the local Darcy permeability. (*d*) A unit cell showing the deformed rectangular fibre array.

The simplified model that we have constructed for the compression of the fibrous network assumes that the fibres in the matrix form a periodic two-dimensional, diamond or rectangular shaped, parallel array perpendicular to the flow direction that compresses linearly with change in gap height, $H - h$, in the vertical direction. Thus, in planes parallel to the lower boundary the fibre spacing Δ_1 remains unchanged, since there is negligible compression in the lateral direction and only Δ_2 changes with the local deformation. Thus,

$$\frac{h}{H} = \frac{2a + \Delta_2}{2a + \Delta_{2H}}, \tag{3.1}$$

where Δ_2 and Δ_{2H} are the deformed and initial vertical fibre spacing, respectively. This type of matrix deformation is reasonable when the solid phase deforms due to the relative boundary motion rather than drag forces arising from the motion of the fluid phase. The motion of the solid phase is neglected. This is a realistic approximation for the endothelial glycocalyx and a reasonable approximation for skiing since the velocity of the skis far exceeds that of the snow powder.

The flow past this periodic, diamond, figure 1(*c*), or rectangular, figure 1(*d*), shaped fibre array is described by the two-dimensional Stokes equations written in terms of the stream and vorticity functions

$$\nabla^2 \psi = \omega, \tag{3.2}$$

$$\nabla^2\omega = 0. \tag{3.3}$$

For the diamond shaped fibre array in figure 1(*c*), the boundary conditions are

$$\psi = \omega = 0 \quad \text{on} \quad \text{BC}, \tag{3.4}$$

$$\frac{\partial\omega}{\partial x} = \frac{\partial\psi}{\partial x} = 0 \quad \text{on} \quad \text{GH, CD}, \tag{3.5}$$

$$\omega = 0, \quad \psi = U\left(a + \frac{\Delta_2}{2}\right) \quad \text{on} \quad \text{FG}. \tag{3.6}$$

In addition, because of the no-slip condition on the fibre post, we require that

$$\psi = \frac{\partial\psi}{\partial n} = 0 \quad \text{on} \quad \text{BH}, \tag{3.7}$$

$$\psi = U\left(a + \frac{\Delta_2}{2}\right), \quad \frac{\partial\psi}{\partial n} = 0 \quad \text{on} \quad \text{DF}, \tag{3.8}$$

in which U is the mean velocity in the x-direction and $\boldsymbol{n}$ is the outward normal unit vector. For the rectangular fibre array arrangement depicted in figure 1(*d*), the corresponding boundary conditions are given by

$$\psi = \omega = 0 \quad \text{on} \quad \text{BC}, \tag{3.9}$$

$$\frac{\partial\psi}{\partial x} = \frac{\partial\omega}{\partial x} = 0 \quad \text{on} \quad \text{CE and GE}, \tag{3.10}$$

$$\omega = 0 \quad \psi = U\left(a + \frac{\Delta_2}{2}\right) \quad \text{on} \quad \text{GE}, \tag{3.11}$$

$$\psi = \frac{\partial\psi}{\partial n} = 0 \quad \text{on} \quad \text{BH}. \tag{3.12}$$

Once the solution for the stream function and vorticity, ψ and ω, are obtained, the dimensionless drag exerted on any given fibre per unit length is given by

$$\frac{F}{\mu U} = a\int_0^{2\pi} [\omega\sin\theta - p\cos\theta]\,\mathrm{d}\theta. \tag{3.13}$$

The Darcy permeability is readily calculated by applying the force balance on a unit cell. This leads to

$$\frac{K_p}{a^2} = \frac{\pi}{c}\frac{\mu U}{F}, \tag{3.14}$$

where c, the solid fibre fraction, is given by

$$c = \frac{2\pi}{\left(2 + \Delta_1/a\right)\left(2 + \Delta_2/a\right)}. \tag{3.15}$$

The dimensionless permeability parameter α in the Brinkman equation is, therefore, given by

$$\alpha = \frac{H}{\sqrt{K_p}} = \frac{H}{a}\sqrt{\frac{Fc}{\mu U\pi}}. \tag{3.16}$$

The pressure p is obtained by integrating the coupled relations

$$\frac{\partial p}{\partial x} = \mu\frac{\partial\omega}{\partial y}, \tag{3.17}$$

$$\frac{\partial p}{\partial y} = -\mu \frac{\partial \omega}{\partial x}. \tag{3.18}$$

In our calculations, equations (3.2) and (3.3) are solved by the method of Sangani & Acrivos (1982). We write general solutions to (3.2) and (3.3) as†

$$\omega = 2\left(4a_1 r - \frac{(4a_1 + 2b_1)a^2}{r(2\ln a + 1)}\right)\sin\theta + 8\sum_{n=2}^{\infty}\sin(2n-1)\theta \times [n a_n r^{2n-1} + (n-1)a^{4n-2}r^{1-2n}(2n a_n - (2n-1)b_n)], \tag{3.19}$$

and

$$\psi = \left[a_1 r^3\left\{1 - \frac{4\ln r}{2\ln a + 1}\left(\frac{a}{r}\right)^2 + \frac{2\ln a - 1}{2\ln a + 1}\left(\frac{a}{r}\right)^4\right\} + b_1 a^2 r\left\{1 - \frac{2\ln r}{2\ln a + 1} - \frac{1}{2\ln a + 1}\left(\frac{a}{r}\right)^2\right\}\right]\sin\theta + \sum_{n=2}^{\infty}\left[a_n r^{2n+1}\left\{1 - 2n\left(\frac{a}{r}\right)^{4n-2} + (2n-1)\left(\frac{a}{r}\right)^{4n}\right\}\right] + b_n a^2 r^{2n-1}\left\{1 - (2n-1)\left(\frac{a}{r}\right)^{4n-4} + 2(n-1)\left(\frac{a}{r}\right)^{4n-2}\right\}\sin(2n-1)\theta. \tag{3.20}$$

Equations (3.19) and (3.20) are expressed in cylindrical coordinates so that the boundary conditions on BC, GH and BH can be satisfied exactly. The unknown coefficients a_n and b_n are determined by applying the remaining boundary conditions in some approximate sense. This is accomplished by a least-square collocation technique adopted in Sangani & Acrivos (1982). We first select a sufficient number of collocation points on either CD, DF and FG for the diamond fibre array, or on CE and EG for the square fibre array, respectively. The boundary conditions are satisfied at discrete points along these remaining boundaries and the resulting linear algebraic equations for a_n and b_n are determined in a least-square sense. The results converge as the number of collocation points increases. We have also solved the biharmonic equation for the stream function using a boundary integral method and obtained results in good agreement with those presented herein.

The dimensionless force exerted on a fibre per unit length is obtained by evaluating the integral in (3.13) using equations (3.17) to (3.20). Note that $G(z) = G(x + \mathrm{i}y) = p - \mathrm{i}\psi$ is an analytic function so that

$$\frac{F}{\mu U} = -\mathrm{Im}\int_{\gamma} G(z)\,\mathrm{d}z = -2\pi \mathrm{Re}[\mathrm{res}(G(z))], \tag{3.21}$$

where res (G) denotes the residues of $G(z)$ within the contour γ, defined by the closed curve $r = a$. It is apparent that both p and ψ have simple poles at $r = 0$ and $G(z)$ has a simple pole at $z = 0$. One finds that, as shown in Sangani & Acrivos (1982), the dimensionless drag per unit length

$$\frac{F}{\mu U} = -\frac{8\pi a^2(2a_1 + b_1)}{2\ln a + 1} \tag{3.22}$$

depends only on the two leading coefficients a_1 and b_1, although their values depend on all the other coefficients. The dimensionless Darcy permeability parameter α is given by (3.16).

In figures 2, 3 and 4 we present the results for both the deformed hexagonal and

† Note there is a typographical error in equation [11] in Sangani & Acrivos (1982).

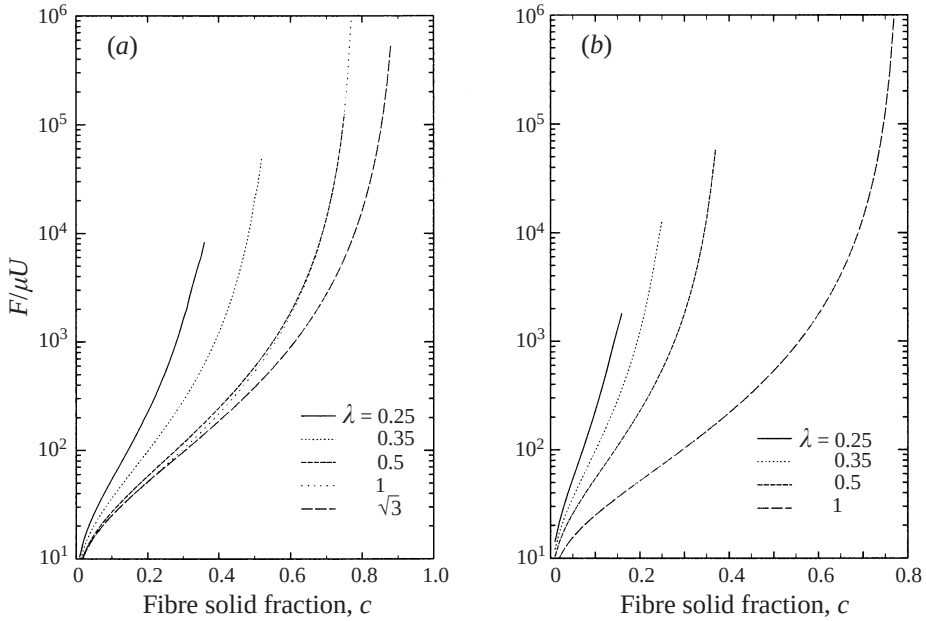

FIGURE 2. The dimensionless drag on a unit length of fibre as a function of fibre solid fraction for different values of $\lambda = (2a + \Delta_2)/(2a + \Delta_1)$. (*a*) Results for diamond shaped fibre array. (*b*) Results for rectangular fibre array.

square fibre arrays. If the results for the fibre drag per unit length are written in terms of the fibre solid fraction c, $F/\mu U$ is independent of the fibre radius and is only a function of the aspect ratio of the fibre array, $\lambda = (2a + \Delta_2)/(2a + \Delta_1)$. Thus in figure 2 we first present general results which are independent of the fibre radius. The fibre solid fraction for the undeformed hexagonal array is twice that of the square array. Figure 2 plots the dimensionless drag $F/\mu U$ as a function of fibre solid fraction c defined by (3.15). These results extend the solutions presented in Sangani & Acrivos (1982) in which only results for $\lambda = \sqrt{3}$, the undeformed hexagonal fibre array, and $\lambda = 1$, the undeformed square array, are presented. As the vertical fibre spacing decreases, the rectangular fibre arrangement experiences monotonically increasing drag on the fibres, as shown in figure 2(*b*). However, this is not true for a diamond shaped fibre array. Because the hexagonal fibre matrix is completely isotropic, the drag for $\lambda = \sqrt{3}$ and $\sqrt{3}/3$ should be the same. Thus, there must be a critical value of λ for which the drag reaches a maximum and the monotonic behaviour with increasing λ cannot be maintained. This is revealed in figure 2(*a*) where the result for $\lambda = 1$ almost overlaps with that for $\lambda = 0.5$.

For application in the microcirculation, where a layer of endothelial glycocalyx seems to be ubiquitous, we calculated the Darcy permeability for a compressed initially hexagonal fibre array whose undeformed fibre spacing $\Delta_1 = 7\,\text{nm}$ and $\Delta_2 = 13\,\text{nm}$. Two fibre radii, $a = 0.6\,\text{nm}$ and $a = 2\,\text{nm}$ are considered herein since they are representative of the sialyic acid side chains in glycosaminoglycans (GAG) and the protein core in proteoglycans, respectively.

The variation of the dimensionless drag as the fibre matrix is compressed vertically is shown in figure 3(*a*) for the initially square and rotated square ($\pi/4$) fibre arrays when the initial fibre spacing, $\Delta_1 = 7\,\text{nm}$, $\Delta_2 = 7\,\text{nm}$ for both arrays. Results are shown for two fibre radii, 0.6 nm corresponding to GAG side chains and 2 nm, typical

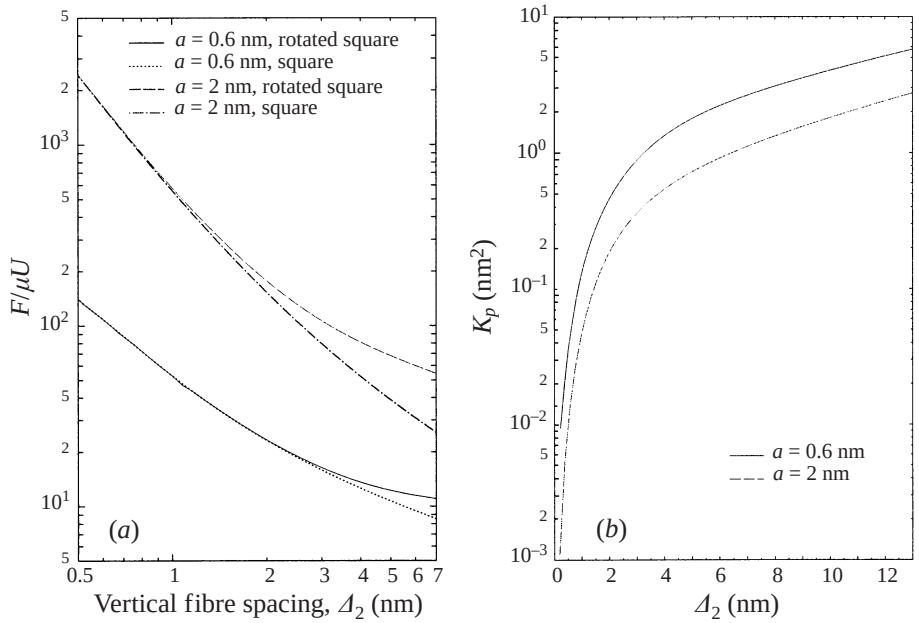

FIGURE 3. (*a*) Increase in the dimensionless fibre drag per unit length as the fibre matrix is compressed vertically for two different fibre radii, $a = 0.6$ nm, GAG side chains in proteoglycans, and $a = 2$ nm, the core protein in a proteoglycan. The undeformed square and rotated square ($\pi/4$) fibre spacing $\Delta_1 = \Delta_{2H} = 7$ nm. (*b*) Variation of the Darcy permeability of the fibre matrix for an initially hexagonal fibre arrangement in which $\Delta_1 = 7$ nm, $\Delta_{2H} = 13$ nm.

of a core protein. As expected the drag increases as Δ_2 decreases. The two sets of curves for a specific fibre radius a converge into a single curve for both arrays as the fibre spacing between adjacent vertical fibres narrows. This is anticipated since, if the fibres are sufficiently close to each other in the vertical direction, the horizontal spacing plays only a minor role in determining the drag exerted on each fibre. Therefore, in the dilute limit when Δ_1 remains fixed and Δ_2 becomes small, the Darcy permeability for a square fibre array will be twice that for a diamond shaped array. Figure 4 exhibits the streamline patterns in a unit cell for the two fibre arrangements. It is clear that the streamlines are squeezed together as λ decreases.

Figure 3(*b*) shows the Darcy permeability for a deformed hexagonal fibre array in which the initial fibre spacings are $\Delta_1 = 7$ nm and $\Delta_{2H} = 13$ nm. Note that this fibre arrangement differs from our previous applications using the fibre matrix model (Weinbaum *et al.* 1992; Fu *et al.* 1994) in which the fibre array is obtained by rotating the square array through $\pi/4$ radians. Most of the calculations presented later in this paper are based on the Darcy permeability shown in figure 3(*b*) for the initially hexagonal fibre array which exhibits a strong nonlinear behaviour as the matrix is compressed. As will be discussed later, this nonlinearity will cause a shift in the pressure distribution and a large increase in the lift force on a moving surface at an attack angle for large matrix deformations. For the endothelial glycocalyx a, Δ_1 and Δ_{2H} are prescribed. Since the local value of Δ_2 depends only on h, see equation (3.1), the variation of K_p as a function of h/H is obtained directly from the curves in figure 3(*b*) using a simple curve fit. For other applications it is a simple matter to construct curves for K_p like those shown in figure 3(*b*) using the results in figure 2 and equation (3.14).

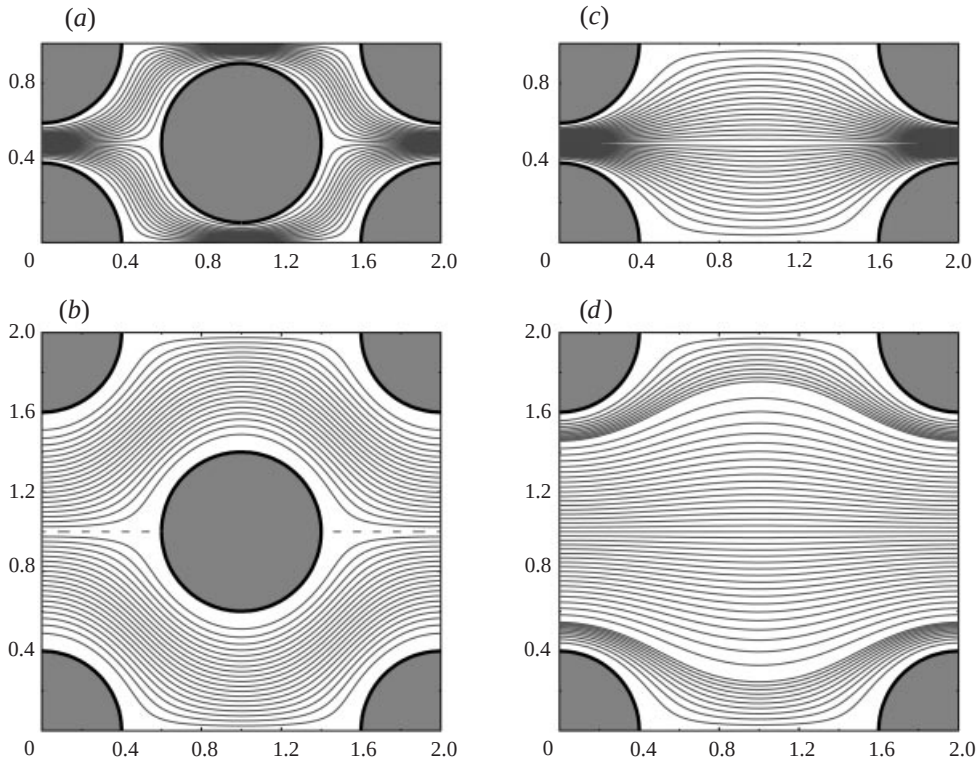

FIGURE 4. Flow patterns within the fibre matrix for both diamond shaped (a, b) and rectangular (c, d) fibre arrays for $\Delta_1/a = 3$, $(2a + \Delta_2)/(2a + \Delta_1) = 1/2$ (a, c) and $(2a + \Delta_2)/(2a + \Delta_1) = 1$ (b, d).

4. One-dimensional analysis: gliding motion of a membrane

In this section, we will apply the one-dimensional lubrication theory developed in § 2 to study the motion of a red cell membrane that penetrates the endothelial glycocalyx. We are also interested in a more general model for an arbitrary one-dimensional surface moving parallel to a fixed planar boundary. We shall show that for this case closed-form solutions can be obtained for the pressure distribution for an arbitrary $h(x)$ provided the boundaries are not deformable. This analysis is a simplified model for many applications in compressible porous media where the leakage of the excess pressure at the lateral boundaries is unimportant. This simple model is also used to illustrate the fundamental new hydrodynamic features that are absent in classical lubrication theory. A related simplified model for an axisymmetric rigid red cell moving in a circular tube lined with a surface glycocalyx is presented in § 6.

We assume that the thickness of the fibre matrix in the fluid gap between the two surfaces is small compared to the characteristic length in the x-direction. This is a reasonable model for a red cell membrane that comes in near contact with the endothelial surface in larger microvessels. We consider first the case of an arbitrary $h(x)$ and show that the one-dimensional Reynolds-type equation (2.25) can be solved exactly. This exact solution will also be used to check the numerical method developed for solving the full two-dimensional equation discussed in the next section.

One notes that equation (2.25) can be integrated directly yielding the general

solution

$$f + \frac{1}{\alpha^2}\frac{\mathrm{d}p}{\mathrm{d}x}(2f - h) = h + C, \tag{4.1}$$

where C is a constant. The constant C is evaluated by prescribing the leading- and trailing-edge pressures. If the pressures at the leading and trailing edges of the cell membrane are the same and α is only a function of x, C can be expressed as

$$C = -\frac{\displaystyle\int_0^1 \alpha^2(h - f)/(2f - h)\,\mathrm{d}x}{\displaystyle\int_0^1 \alpha^2/(2f - h)\,\mathrm{d}x}. \tag{4.2}$$

The pressure distribution from (4.1)is given by

$$p - p_0 = \int_0^x \frac{\alpha^2(h - f + C)}{2f - h}\mathrm{d}x, \tag{4.3}$$

where p_0 is the pressure at $x = 0$ and $x = 1$ if C is given by (4.2).

To examine the asymptotic behaviour of the pressure distribution in the fibre matrix when α is large, we notice from (2.20) that in this limit $f \sim \alpha^{-1}$. If we expand the integrands in both equations (4.2) and (4.3), we obtain the following expressions which are valid for large α:

$$C = -\int_0^1 \alpha^2 \mathrm{d}x \Big/ \int_0^1 \frac{\alpha^2}{h}\mathrm{d}x, \tag{4.4}$$

$$p - p_0 \sim -\int_0^x \frac{\alpha^2(h + C)}{h}\mathrm{d}x. \tag{4.5}$$

If matrix compression were neglected and α were a constant $p - p_0$ would be proportional to α^2. Our numerical results, which we present later in figure 15, show that this power dependence on α is also approximately valid for the total lift force for $\alpha > 10$.†

The total dimensionless lift force F is obtained by integrating (4.3) over the entire surface. This leads to

$$F = \int_0^1 (p - p_0)\,\mathrm{d}x = \int_0^1 (1 - x)\frac{\alpha^2(h - f + C)}{2f - h}\mathrm{d}x, \tag{4.6}$$

where we have changed the order of integration in evaluating the double integral. The velocity components, flow patterns and drag force on the membrane can be calculated in a manner similar to that for classical lubrication theory. In general α will be a highly nonlinear function of h as quickly surmised from figure 3(*b*). Once $h(x)$ is prescribed, equations (4.2) and (4.3) provide a remarkably simple solution for the pressure distribution in the compressed matrix layer for any $h(x)$. This will greatly facilitate the treatment of deformable surfaces using iterative methods.

To illustrate the general behavior, we performed numerical calculations for a simple example in which an inclined planar surface of length L moves at a constant velocity over a thin fibre matrix. The undeformed thickness of the matrix is assumed to be h_2 and the compression ratio k is defined by the ratio h_2/h_1, where h_1 is the compressed matrix thickness at the trailing edge. Typical solutions for the pressure distribution

† The authors wish to thank Professor Howard A. Stone for bringing to our attention the asymptotic behaviour of the pressure field that scales as α^2 for large values of α and the derivation of equation (4.5).

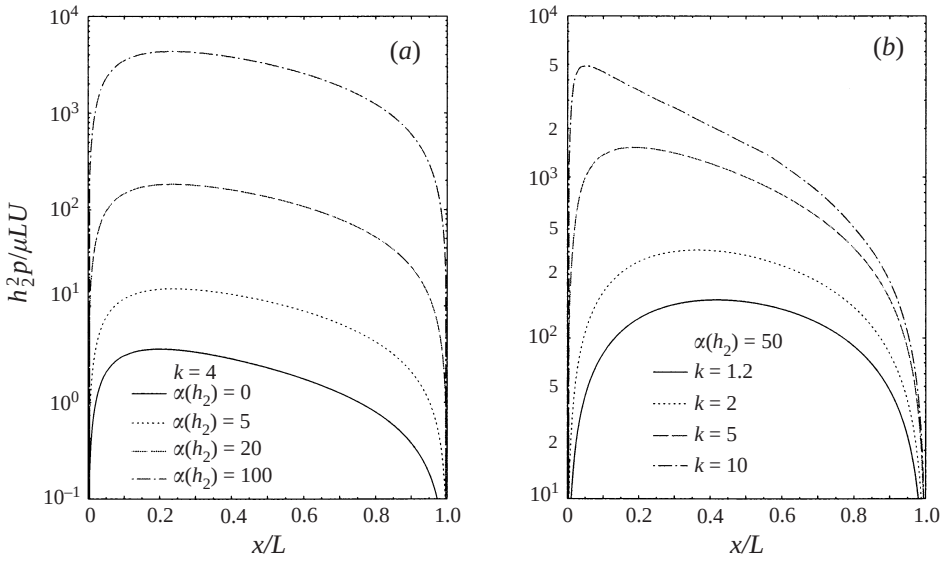

FIGURE 5. Dimensionless pressure distribution in a compressed fibre matrix. (*a*) Pressure for different values of the undeformed $\alpha(h_2)$ in which the compression ratio $k = 4$. (*b*) Pressure for various compression ratios k in which $\alpha(h_2) = 50$, a value close to that predicted for a 100 nm thick glycocalyx with an initially undeformed hexagonal fibre array in which $\Delta_1 = 7$ nm, $\Delta_{2H} = 13$ nm and $a = 0.6$ nm.

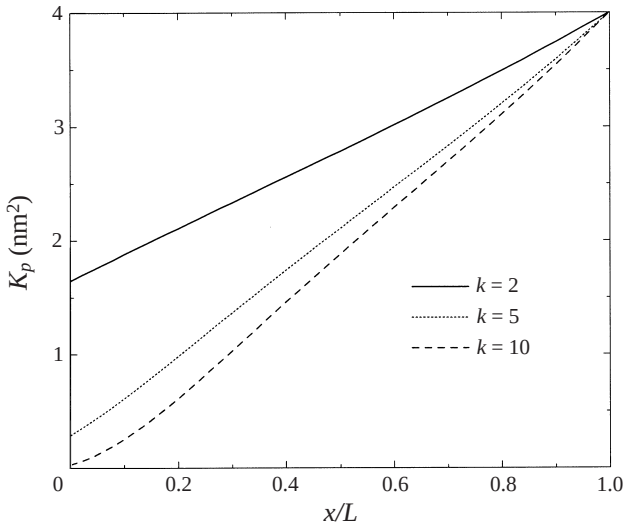

FIGURE 6. Spatial variation of K_p for a 100 nm thick undeformed fibre matrix under various compression ratios.

beneath this planar surface are shown in figure 5. Here the undeformed thickness h_2 and $\alpha(h_2)$ at the leading edge are prescribed. The slope of the plane $(h_2 - h_1)/L$ is given in terms of the matrix compression ratio, $k = h_2/h_1$, as $(1 - 1/k)h_2/L$, see figure 1. In figure 5(*a*), the pressure distribution for a moderately compressed matrix, $k = 4$, is plotted for several increasing values of the undeformed permeability parameter

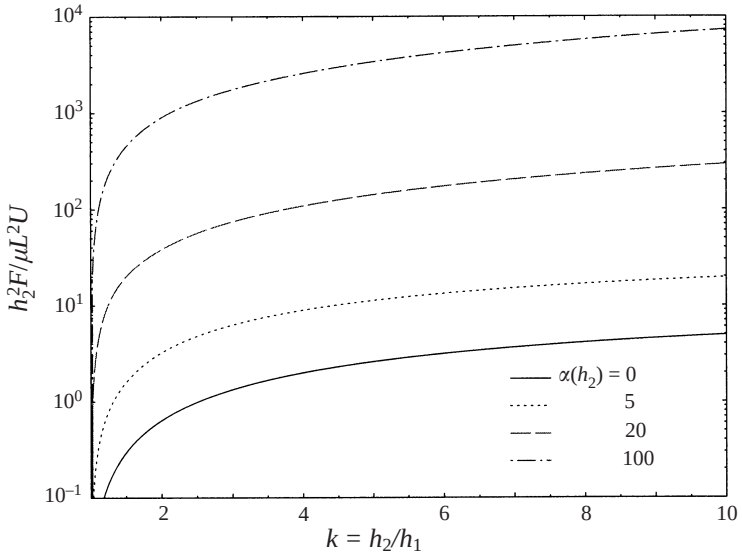

FIGURE 7. The dimensionless lift force on a moving planar boundary as a function of compression ratio k for different values of $\alpha(h_2)$.

$\alpha(h_2)$. Also shown for comparison are the predictions of classical lubrication theory, the limiting case of (2.25) when $\alpha = 0$. It is observed that the pressure increases remarkably as $\alpha(h_2)$ increases from zero, a pure fluid layer, to $\alpha(h_2) = 100$. The pressure generated within the matrix for $\alpha(h_2) = 100$ is three orders of magnitude greater than for $\alpha = 0$. Figure 5(b) shows the change in the pressure distribution as the matrix compression ratio is increased when $\alpha(h_2) = 50$, a value representative of a 100 nm thick endothelial glycocalyx. The maximum possible compression ratio is about 12. To illustrate how K_p varies with position and the compression ratio k we have plotted in figure 6 the variation of K_p from leading to trailing edge for three of the pressure profiles shown in figure 5(b). There is significant nonlinear variation of K_p near the trailing edge only for the largest value of k, namely $k = 10$. The large decrease in K_p from leading to trailing edge produces a pronounced shift in the maximum pressure towards the trailing edge for large values of k, see figure 5. The combined results in figure 5(a, b) lead to the dramatic increase in the integrated lift force shown in figure 7, where the dimensionless lift force is plotted as a function of k. We note that the total lift force on the moving surface increases as the compression ratio k increases, due to the large increase in α as one approaches the trailing edge. This is in contrast to the well-known result in classical lubrication theory for a slider bearing where the lift force is a maximum when $h_2 \approx 2.2h_1$ and h_1 is fixed.

It is also of interest to plot the position of the maximum pressure x_m/L as a function of k for different values of $\alpha(h_2)$. This is shown in figure 8, where we notice that x_m/L exhibits a more complicated behaviour than the lift force. For small values of $\alpha(h_2)$, the maximum pressure is achieved closer to the midpoint than for $\alpha = 0$, the pure fluid layer. However, as $\alpha(h_2)$ increases there is a large shift in the position of the maximum pressure towards to the trailing edge of the plate as k increases. For the purpose of comparison, we have also calculated x_m/L if the matrix compression is neglected, i.e. $\alpha = \alpha(h_2)$ throughout the matrix. The results show that there is a much larger shift in the pressure maximum toward the trailing edge when matrix compression is considered. This is due to the large nonlinearity in the Darcy

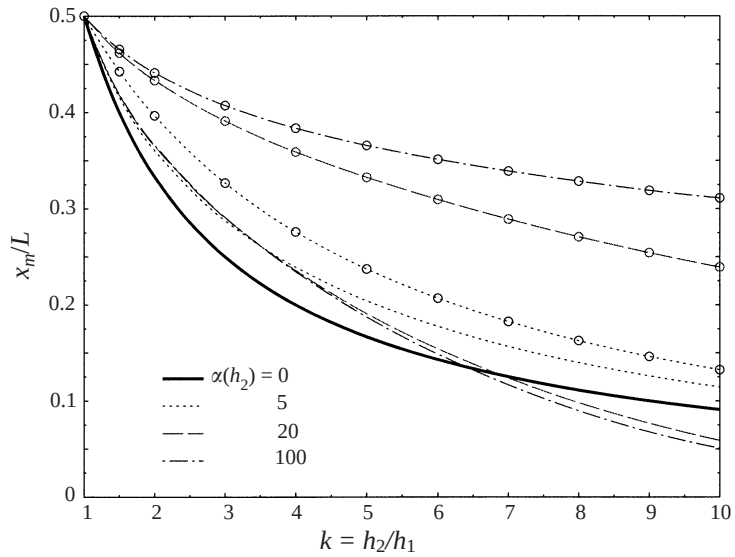

FIGURE 8. Shift of the maximum pressure on the moving surface. For comparison, results for constant α throughout the matrix are shown by circles. The thick solid curve is the result for a pure fluid layer.

permeability that develops as the matrix is compressed near the trailing edge. This gives rise to the large asymmetry in the pressure profile shown in figure 5. Figure 8 also indicates that x_m/L is nearly independent of $\alpha(h_2)$ once $\alpha(h_2)$ exceeds 20 for all values of k.

Figure 9 illustrates the change in the streamline pattern as $\alpha(h_2)$ increases. For $\alpha = 0$ there is a small recirculation region near the trailing edge where the pressure gradient is negative. However, as $\alpha(h_2)$ increases, a dividing streamline develops starting near the trailing edge and fluid is either expelled in front of the leading edge or ejected at the trailing edge of the moving surface. This behaviour is more easily interpreted in terms of the velocity profiles exhibited in figure 10, where horizontal velocity profiles are presented at three positions: the leading edge $x/L = 1$, the trailing edge $x/L = 0$ and x_m/L, the position of the pressure maximum. The velocity component is normalized relative to the sliding velocity U. In sharp contrast to a pure fluid layer, $\alpha = 0$, the horizontal velocity remains almost constant in the central region of the matrix for large values of α, except for a thin transition layer near the boundaries where the no-slip condition must be satisfied. In fact, as the Darcy term becomes larger and dominates the effect of the viscous dissipation terms, the Brinkman medium reduces to a Darcy medium in which a uniform plug flow proportional to the local pressure gradient is anticipated. Therefore, the Brinkman medium bridges the transition from a slow viscous creeping flow characteristic of classical lubrication theory to a Darcy flow which satisfies a potential equation for the pressure field and no-slip conditions cannot be satisfied. This transition in behaviour was also observed by the authors in a recent study of the flow through a circular orifice in a Brinkman medium (Feng & Weinbaum 2000). Although not shown, one finds that at large α the bulk motion in the central region is small and it is only near the leading and trailing edges, where the pressure gradient is large, that there is a significant bulk flow.

The key result of this section is the large increase in the pressure generated within the fibre matrix as $\alpha(h_2)$ increases. In the microcirculation, this would result in a

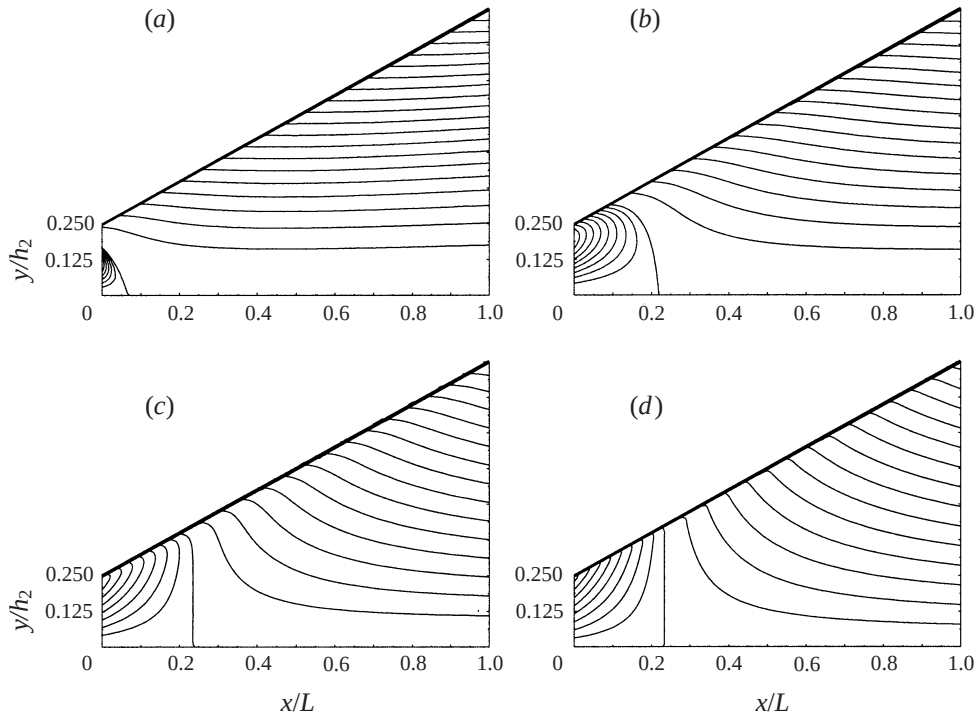

FIGURE 9. Streamline patterns within the fibre matrix for four increasing values of the permeability parameter $\alpha(h_2)$. (*a*) $\alpha = 0$, classical lubrication theory, (*b*) $\alpha(h_2) = 5$, (*c*) $\alpha(h_2) = 20$, (*d*) $\alpha(h_2) = 100$. The fibre matrix is described by the same parameters as in figure 5.

huge repulsive force on a moving red cell if it attempted to penetrate the endothelial glycocalyx and its membrane did not deform. Thus, even in larger arterioles and venules where the red cells may not move in single file, one would expect to see a small clearance between the red cell and the outer edge of the surface glycocalyx. This prediction is consistent with the recent observations of Henry & Duling (1999) where a thin fluid layer of 0.2 to 0.5 μm was measured in 10–15 μm diameter vessels. The glycocalyx, though highly compressible, provides a protective barrier that prevents adhesive interactions between the red cell and endothelial membranes and hence prolongs the life time of the red cell.

5. Motion of a ski or snowboard

While the motion of red cells inside a microvessel provided the initial motivation for this study, the behaviour of the red cell has a striking similarity to the gliding motion of a ski or a snowboard on a thin layer of compressed dry powder. In this section, we propose a two-dimensional fibre matrix model to analyse the mechanics of skiing. Figure 11 is a schematic illustration of a ski or a snowboard on a thin layer of dry powder, which is described by the Brinkman equation. A Cartesian coordinate system is chosen in which the z-axis is in the vertical direction. We consider a rectangular shaped ski or snowboard whose length and width are L and W, respectively. We assume that the thickness of the lubricating layer does not vary in the y-direction and is only a function of x. This implies that the permeability parameter α is also independent of y. The sliding velocity is denoted by $U\boldsymbol{i}_x$. The primary difference

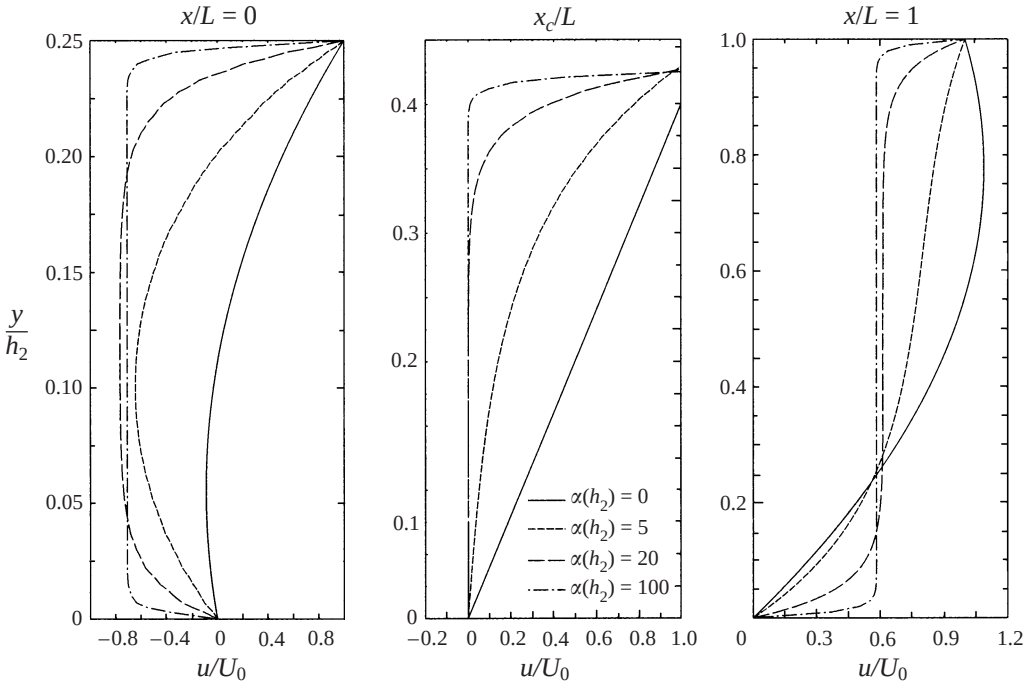

FIGURE 10. Normalized horizontal velocity profiles in fibre matrix for representative $\alpha(h_2)$. Three sets of profiles are shown which correspond to the leading and trailing edges and the position where the pressure reaches its maximum, x_m/L.

between the red cell and the ski lies in the substantial pressure loss from the leakage at the lateral edges of the skis, which is absent for a red cell if its membrane fills the entire vessel circumference. While there are experimental data for the permeability of snow under various conditions (Arons & Colbeck 1995; Jordan *et al.* 1999), there are no data for how its permeability changes under compression. We, therefore, use the same fibre matrix model as described in § 3 for the endothelial surface glycocalyx to estimate the variation of α with h without any further attempt to model the detailed crystal structure of the snow flakes. Our purpose is to provide a simple prototype model to obtain some insight into this complicated problem. It is also emphasized that for a ski the assumption that $h/W \ll 1$ is likely to be violated except for very thin layers of compressed powder. The theory in its present form is more applicable to a snowboard or toboggan. A different type of analysis needs to be developed for a ski in which inertial effects are considered in the transverse direction and a centreline theory is used to describe the axial pressure distribution.

By introducing the characteristic variables defined in § 2, one can write the dimensionless Reynolds-type equation (2.23) for the pressure within the powder as

$$\frac{\partial}{\partial x}\left[f + \frac{1}{\alpha^2}\frac{\partial p}{\partial x}(2f - h)\right] + \frac{L^2}{W^2\alpha^2}(2f - h)\frac{\partial^2 p}{\partial y^2} = \frac{\partial h}{\partial x}. \tag{5.1}$$

Equation (5.1) is a second-order elliptic partial differential equation which needs to be solved numerically. We have developed a numerical method based on the pseudo-spectral collocation technique of Orszag (1971).

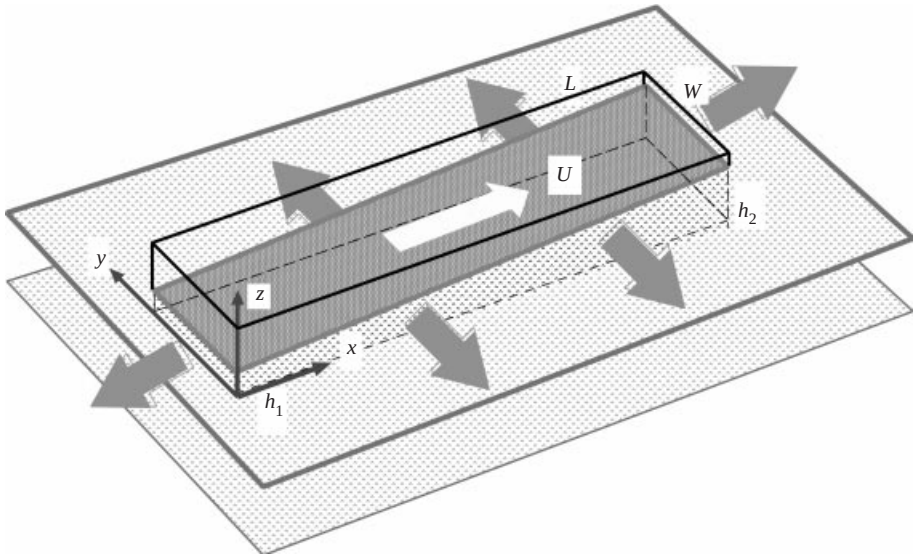

FIGURE 11. Schematic illustration of a snowboard or ski compressing a thin layer of fresh powder. Note the escape of air at lateral edges.

5.1. *Numerical solution of the Reynolds-type equation*

In order to solve the Reynolds equation (5.1), we expand the pressure in a double series defined on the domain $D = [0,1] \times [0,1]$ as

$$p(x,y) = \sum_{n=0}^{\infty} \sum_{m=1}^{\infty} p_{nm} T_n(2x-1) \sin(2m-1)\pi y, \tag{5.2}$$

in which p_{nm} are unknown coefficients and T_n is a Chebyshev polynomial of order n. Solution (5.2) already satisfies the boundary conditions at $y = 0$ and $y = 1$. When (5.2) is substituted into (5.1) and the orthogonality of the sine function is employed, one obtains the following set of algebraic equations for p_{nm}

$$\sum_{n=0}^{\infty} p_{nm} \left(\frac{2f-h}{\alpha^2} \left[\frac{\mathrm{d}^2}{\mathrm{d}x^2} T_n(2x-1) - \frac{L^2}{W^2} T_n(2x-1) \right] + \frac{\mathrm{d}}{\mathrm{d}x} \frac{2f-h}{\alpha^2} \cdot \frac{\mathrm{d}}{\mathrm{d}x} T_n(2x-1) \right)$$
$$= \left(1 - \frac{1}{k} - \frac{\partial f}{\partial x} \right) \frac{4}{(2m-1)\pi}, \quad m = 1, 2, \ldots . N. \tag{5.3}$$

Using the orthogonality of the Chebyshev polynomial, one can express the derivatives of $T_n(x)$ appearing in (5.3) in terms of Chebyshev polynomials. The details of the required formulae can be found in the appendix of Orszag (1971).

We choose the first M equations in (5.3) and truncate the infinite summation at its $N+2$ term, where N is sufficiently large to ensure the convergence of the solution. The coefficients p_{nm} are obtained by applying equation (5.3) at N collocation points which are the zeros of $T_N(x)$. These algebraic equations are combined with the boundary condition $p(0) = p(1) = 0$ to solve for the $N + 2$ coefficients for a given m. The numerical scheme is quite stable and convergent as N increases compared with the solution expressed in a double Fourier series.

In our calculations, we use $M = 50$ and $N = 100$. The pressure at the centre point of the snowboard varies within 0.1% for $M \geqslant 100$ and $N \geqslant 200$. The numerical

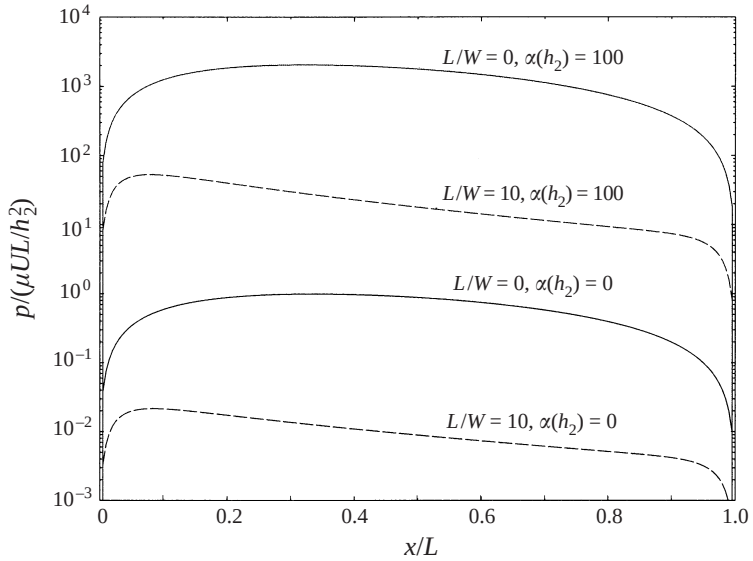

FIGURE 12. Comparison of the pressure distribution on the centreline of a ski or snowboard for an intermediate value of $L/W = 10$ and on an infinitely wide surface, $L/W = 0$, with no leakage of air at the lateral edges. In both cases $k = h_2/h_1 = 2$. The thickness of the compressed snow powder at the leading edge is assumed to be 2 cm and the value of α at this location, $\alpha(h_2) = 100$, a value typical of moderately packed fresh snow. In the absence of experimental data for the variation of K_p with compression for snow, we have applied the same simple fibre model as sketched in figure 1 for the endothelial glycocalyx.

results for the pressure at $y = 1/2$ when $W/L > 20$ are in excellent agreement with the exact solution presented in the previous section for $W/L \to \infty$.

5.2. *Results and discussion*

To facilitate comparison with the one-dimensional solution the results for the pressure are presented only at the centreline of the ski or snowboard, $y = 1/2$. One of the most important parameters in this application is the choice of the undeformed Darcy permeability for fresh snow powder. Here we assume that the powder is composed of a fibrous matrix whose effective fibre radius a is 0.1 mm. However, as shown in figure 3 the results are not very sensitive to the value of a. For the purpose of illustrating how large a pressure can be built up beneath a ski or snowboard, we will present results for various values of $\alpha(h_2)$. The actual value of the fibre spacing at the leading edge, and hence the value of $\alpha(h_2)$, in the present model has to be determined by requiring that the total lift force generated by the compressed powder be equal to the weight of the skier and his/her skis. We shall find that representative values of $\alpha(h_2)$ that are required to support a 70 kg human increase from 100 to 400 as the compression ratio k decreases from 5 to 2. The Darcy permeability K_p predicted by our fibre matrix model varies between 2.5×10^{-9} m^2 for $\alpha(h_2) = 400$ and 4×10^{-8} m^2 for $\alpha(h_2) = 100$. These predicted values lie in the same range as the measured values, 10^{-9} to 10^{-8} m^2, for snow under various conditions (Jordan *et al.* 1999).

The fundamental difference between a red cell gliding on the endothelial glycocalyx and the human skiing on fresh powder is schematically shown in figure 11. For the skier or snowboarder there can be a very large loss in the excess pressure due to the escape of the air at the lateral edges of the planing surface. The magnitude of this

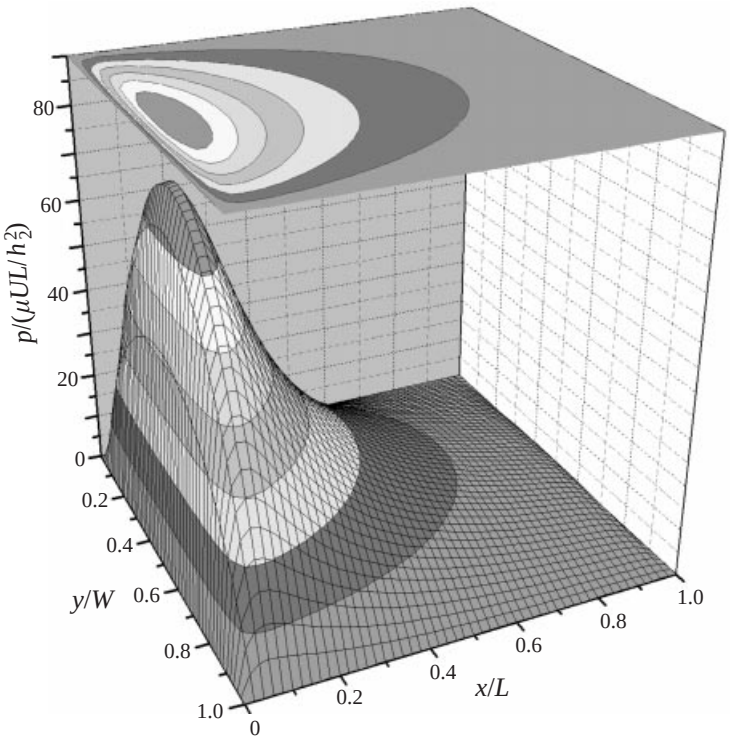

FIGURE 13. Pressure distribution and equal pressure contours under a snowboard. The aspect ratio is $L/W = 10$ and the thickness of undeformed snow powder is 2 cm. $\alpha(h_2) = 100$.

loss in excess pressure is largely determined by the parameter L/W in the second term in equation (5.1). For straight skis a typical of value of L/W is 20, whereas for a snowboard it is closer to 5. In either case $L^2/W^2 \gg 1$. We illustrate the essential physics by presenting results for the pressure distribution for $L/W = 10$ in figure 12 for $k = 2$, a moderate compression, for both $\alpha = 0$ (classical lubrication theory) and $\alpha(h_2) = 100$, a value representative of moderately packed snow powder. Also shown for comparison are the results for $L/W = 0$, the case where there is no leakage at the lateral edges, as for the tightly fitting red cell. One observes that the dimensionless excess pressure beneath a planar surface with $L/W = 10$ is two orders of magnitude smaller than for $L/W = 0$. However, for $L/W = 10$ there is a large shift in the maximum pressure towards the rear of a ski or snowboard even at this moderate value of k. The pressure builds up gradually over most of the length of the ski and there is a sharp drop near the trailing edge. This asymmetric pressure distribution would exert a large torque on the skier's ankles and the skier would adjust to a smaller angle of attack.

Figure 13 shows the dimensionless two-dimensional pressure distribution and equal pressure contours under a typical snowboard which has aspect ratio $L/W = 10$. Note that the variation of pressure is almost linear in the logarithmic plot in figure 12, except near the leading and trailing edges, indicating that the pressure decays exponentially in the longitudinal direction from its peak value near the trailing edge. However, the transverse pressure distribution exhibits a parabolic behaviour at any longitudinal location along the snowboard. In fact, one can assume a parabolic pressure profile

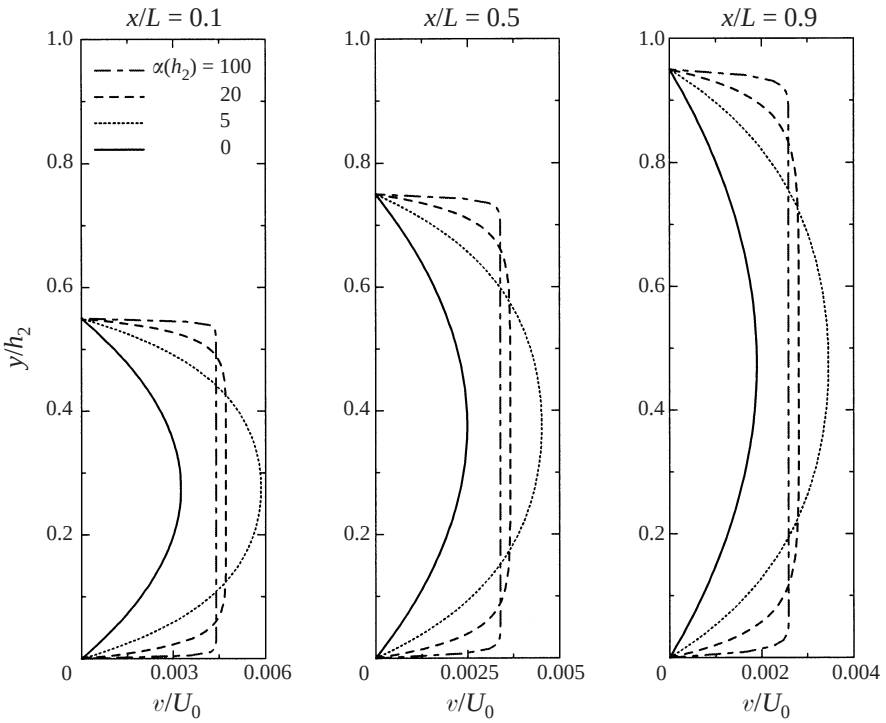

FIGURE 14. Normalized transverse velocity profiles in the fibre matrix at the lateral edge of a snowboard for representative $\alpha(h_2)$ for compression ratio $k = 2$. Three sets of profiles are shown at $x/L = 0.1$, 0.5 and 0.9 and $y/W = 0$ or 1.

in the transverse direction and reduce the two-dimensional generalized Reynolds equation to an equivalent one-dimensional equation, using a centreline theory that assumes a simplified family of transverse pressure profiles.

It is also of interest to examine the velocity profile in the transverse direction at the lateral edges $y/W = 0$ and 1 of the snowboard. One anticipates that these profiles exhibit some form of slip condition similar to the well-known Joseph–Beaver slip condition since the snowboard is sliding relative to the fixed porous medium. For this purpose we present three transverse velocity profiles in figure 14 at $x/L = 0.1$, 0.5 and 0.9, corresponding to the rear, central and front edges, respectively. Note that the transverse velocity vanishes at $x/L = 0$ or 1 since constant pressure is assumed outside the Brinkman layer. Figure 14 clearly shows a slip-type behaviour as the Darcy permeability decreases. The magnitude of the velocity is of the same order for all values of $\alpha(h_2)$. As α increases, both the lateral pressure gradient and the hydraulic resistance of the matrix increase, yielding edge profiles that drastically change in shape, but not magnitude.

Figure 15 provides an overall comparison of the changes in lift or repulsive forces as α increases for a planar surface with $L/W = 0$ and $L/W = 10$. The transition for the large increase in lift due to the porous medium occurs at α order one. For the red cell the value of α at the leading edge, $\alpha(h_2)$, where the membrane first penetrates the glycocalyx is 160 based on a 0.4 μm thickness for the undeformed matrix and an open gap between fibres of 7 nm. For a human skier or snowboarder the value of α at the leading edge is determined by the requirement that the total lift force must

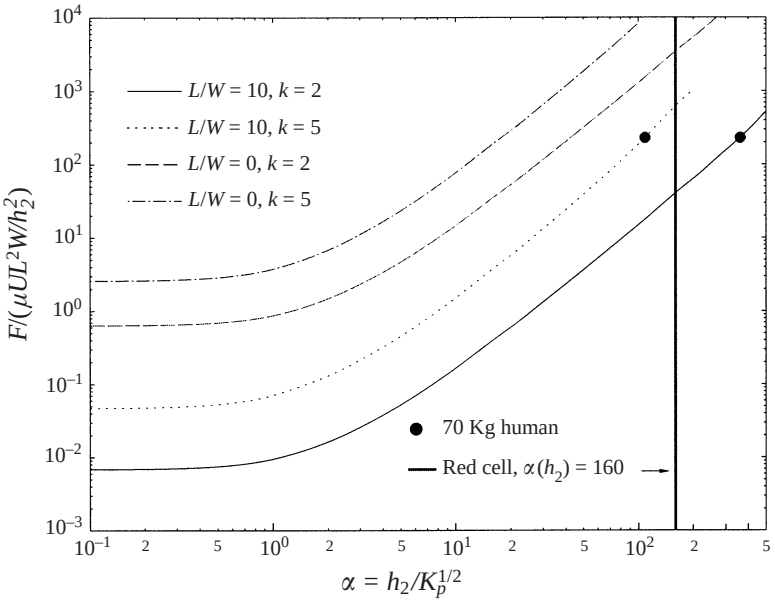

FIGURE 15. Increase in the dimensionless lift force as the value of α at the leading edge, $\alpha(h_2)$, increases. For a red cell, $L/W = 0$, $h_2 = 0.4\,\mu\text{m}$, $\Delta_1 = 7\,\text{nm}$ and $\alpha(h_2) = 160$. The properties of the endothelial glycocalyx away from the leading edge are described by the curve for $a = 0.6\,\text{nm}$ in figure 3. For a human skiing on a planar surface with $L/W = 10$, we require that the value of $\alpha(h_2)$ be chosen such that the lift force supports a 70 kg person when $L = 150\,\text{cm}$. The critical value of α depends on the compression ratio, $k = h_2/h_1$, of the surface. If $h_2 = 2\,\text{cm}$, $\alpha(h_2) \sim 400$ for $k = 2$ and $\alpha(h_2) \sim 100$ for $k = 5$.

equal the weight of the skier plus his/her equipment. The value of α at the leading edge required to achieve this lift will depend on k, the compression ratio, and, as observed in figure 15, will decrease from about 400 to 100 as k increases from 2 to 5. By digging one's heels into the snow one can achieve the same lift with a small compression at the leading edge and a large compression at the trailing edge. This will also lead to a much larger drag force (not shown).

6. Pressure-driven flow of a red cell in a capillary

The results of the analysis presented in § 4 have important implications for the *in vivo* rheology of blood in the microcirculation in which the endothelial glycocalyx plays a vital role. We are interested, in particular, in the role of the endothelial surface glycocalyx in determining the rheological properties of blood and the pop out phenomenon in which the red cell will rise off the endothelial surface and then glide near the edge of the surface matrix layer. Although limited experimental data are available on the material properties of the glycocalyx, the fibre matrix model based on the Brinkman equation has been applied to several biological transport problems where it has successfully predicted the measured hydraulic and diffusive permeability coefficients (Weinbaum *et al.* 1992; Fu *et al.* 1994; Weinbaum 1998; Hu & Weinbaum 1999). The advantage of the Brinkman equation lies in its simplicity and that one does not need detailed knowledge of the glycocalyx structure to estimate K_p. We can thus use the model in § 3 to represent the fibre deformation. Although this model is based on a flow transverse to a periodic fibre array, these results compare quite well

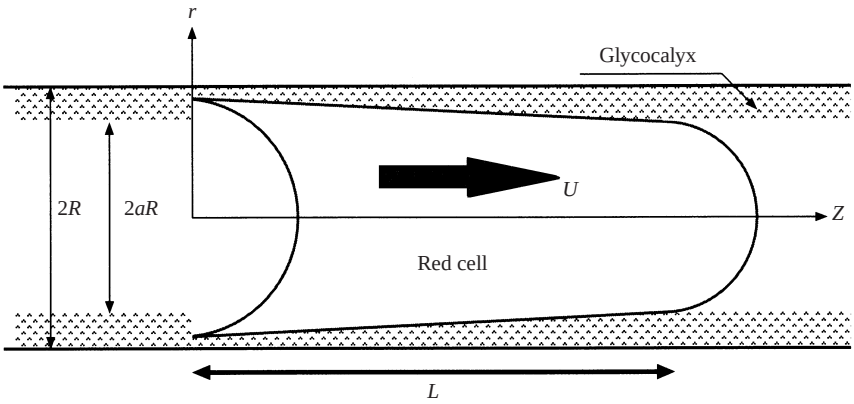

FIGURE 16. Axisymmetric motion of a deformed red cell in a capillary lined with endothelial surface glycocalyx. The model assumes that the red cell penetrates into the surface glycocalyx and two spherical caps are attached to its front and rear to ensure that the surface and volume are unchanged during deformation.

with those for a randomly distributed fibre matrix (Ethier 1991). We first present a simple geometric model for the pressure-driven motion of an idealized red cell which penetrates into the glycocalyx and then examine the effect of this motion on the tube hematocrit and apparent viscosity.

6.1. *Model and formulation*

There have been numerous previous models for the motion of red cells in microvessels (Lighthill 1968; Fitz-Gerald 1969; Tozeren & Skalak 1978; Secomb *et al.* 1986; Damiano 1998; Secomb *et al.* 1998). Early studies used classical lubrication theory to describe the fluid layer near the capillary wall. The most recent investigations have applied mixture theory to describe a glycocalyx with no deformation and, with the exception of Secomb *et al.* (1998), have assumed that the red cell membranes do not penetrate the glycocalyx. Secomb *et al.* (1986) have shown that axisymmetric lubrication theory yields very accurate results for rigid spheres even for moderate sphere-to-tube diameter ratios. We thus wish to generalize the analysis in § 2 to treat the axisymmetric motion of a rigid pellet in a circular tube which has a deformable matrix lining its walls, as illustrated in figure 16. The simplified shape assumed for the red cell pellet in figure 16 is a cylinder with a linearly varying radius with hemispherical caps at both its front and rear surfaces. The length of the cell and the size of the caps are determined by requiring the surface area and the volume of the red cell, which in our calculation, are 141.6 μm^2 and 91.5 μm^3, respectively, to remain constant. A uniform pressure is applied at both the front and rear surfaces and the spherical cap at the front enters the matrix where the sidewall starts. The pellet dimensions are shown in figure 16 for a 5 μm diameter capillary in which the surface glycocalyx is 0.4 μm thick and $k = 2$. We are primarily interested in the effect of varying k on the pellet motion. In this highly idealized model the deformation of the red cell is neglected.

The dimensionless Brinkman equation in cylindrical coordinates is given by

$$\frac{1}{r'}\frac{\partial}{\partial r'}\left(r\frac{\partial u_z'}{\partial r'}\right) = \frac{\partial p'}{\partial z'} + \alpha^2 u_z', \tag{6.1}$$

where the dimensionless primed variables are defined by

$$u_z' = \frac{u_z}{U_c}, \quad r' = \frac{r}{R}, \quad z' = \frac{z}{R}, \quad p' = \frac{P}{\mu U_c L/R^2}. \tag{6.2}$$

Here R is the vessel radius and U_c is the translational velocity of the red cell. The permeability parameter α is now defined as

$$\alpha = \frac{R}{\sqrt{K_p}}. \tag{6.3}$$

For convenience, we now drop the prime on the dimensionless quantities.

The solution to (6.1) which satisfies the no-slip boundary conditions on the capillary wall and the cell surface closely parallels the derivation in Damiano *et al.* (1996) except that no intervening fluid layer is present between the red cell and the edge of the glycocalyx. The axial velocity is given by

$$u_z = A\left[I_0(\alpha r) - \frac{I_0(\alpha)}{K(\alpha)}K_0(\alpha r)\right] + \frac{1}{\alpha^2}\left[\frac{K_0(\alpha r)}{K_0(\alpha)} - 1\right]\frac{\mathrm{d}p}{\mathrm{d}z}, \tag{6.4}$$

where

$$A = \frac{1 - \dfrac{1}{\alpha^2}\left[\dfrac{K_0(\alpha r_c)}{K_0(\alpha)} - 1\right]\dfrac{\mathrm{d}p}{\mathrm{d}z}}{I_0(\alpha r_c) - \dfrac{I_0(\alpha)}{K_0(\alpha)}K_0(\alpha r_c)}.$$

Here $r_c(z)$ denotes the shape of the red cell and I and K are modified Bessel functions. When equation (6.4) is substituted into the continuity equation and integrated, one obtains

$$\frac{q_0}{2} = \frac{r_c^2}{2} + \int_{r_c}^{1} u_z(r, z) r \, \mathrm{d}r, \tag{6.5}$$

where q_0 is the total flux through the cross-section normalized by $U_c R^2$. Substituting (6.4) into (6.5), one obtains the following Reynolds-type equation for an arbitrary axisymmetric red cell flowing through a circular tube coated by a layer of fibre matrix:

$$\frac{\mathrm{d}p}{\mathrm{d}z} = \frac{Rq_0 - \frac{1}{2}r_c^2 + C/D}{B + \dfrac{1}{\alpha^2}\left[\dfrac{K_0(\alpha r_c)}{K_0(\alpha)} - 1\right]C/D}. \tag{6.6}$$

Here the auxiliary functions B, C and D are given by

$$B = \frac{r_c^2 - 1}{2\alpha^2} + \frac{1}{\alpha^3 K_0(\alpha)}[r_c K_1(\alpha r_c) - RK_1(\alpha)],$$

$$C = \frac{RI_1(\alpha) - r_c I_1(\alpha r_c)}{\alpha} + \frac{I_0(\alpha)}{\alpha K_0(\alpha)}[RK_1(\alpha) - r_c K_1(\alpha r_c)],$$

$$D = I_0(\alpha r_c) - \frac{I_0(\alpha)K_0(\alpha r_c)}{K_0(\alpha)},$$

respectively. Note that in (6.6) r_c is a function of z and that α is determined by the local compression of the matrix layer. In order to determine the pressure distribution, q_0 has to be prescribed. If the red cell is freely suspended, the total applied force has to vanish. This zero-drag condition, which we describe next, uniquely determines the motion.

We choose a control volume, bounded by two cross-sections at $z = 0$ and $z = L$ in figure 16 and the corresponding segment of tube wall. Since the freely suspended red cell does not exert a net force, the total force applied on this control volume must be zero for steady flow. Integrating the Brinkman equation over any volume ($\mathscr{V}$), we obtain the following relation:

$$\int\int_{\partial\mathscr{V}} \mu \frac{\partial \boldsymbol{u}}{\partial n} \mathrm{d}S - \int\int\int_{\mathscr{V}} \frac{\mu}{K_p} \boldsymbol{u} \mathrm{d}V = \int\int_{\partial\mathscr{V}} p\boldsymbol{n} \mathrm{d}S, \tag{6.7}$$

where $\boldsymbol{n}$ is the normal unit vector of the control volume. Note the second term, which is absent for Stokes flow, represents a body force within the control volume. This force is balanced by the drag force on the fibres.

When equation (6.7) and the lubrication approximation are applied, one finds that

$$2\pi \int_0^L \left[\frac{1}{2} \frac{\mathrm{d}p}{\mathrm{d}z} - \tau_w - \alpha^2 \int_{r_c}^1 ur \, \mathrm{d}r \right] \mathrm{d}z = 0, \tag{6.8}$$

where τ_w, the shear stress exerted on the tube wall from (6.4), is given by

$$\begin{aligned} \tau_w &= \mu \left. \frac{\partial v_z}{\partial r} \right|_{r=R} \\ &= -\frac{K_1(\alpha R)}{\alpha K_0(\alpha R)} \frac{\mathrm{d}p}{\mathrm{d}z} + A\alpha \left[I_1(\alpha R) + \frac{I_0(\alpha R) K_1(\alpha R)}{K_0(\alpha R)} \right]. \end{aligned} \tag{6.9}$$

The Reynolds equation, together with the zero-drag condition (6.8) are sufficient to solve for the pressure distribution and the total flux q_0.

6.2. *Results and discussion*

We assume that the glycocalyx can be modelled by the fibre matrix structure described in § 3. For comparison with previous studies, we consider a red cell flowing through a 5 μm capillary coated by a 0.5 μm thick glycocalyx as shown in figure 17. Theoretical predictions for the dimensional pressure distribution along the tube axis for a red cell velocity of $0.1\,\mathrm{cm\,s^{-1}}$ are shown in the upper portion of figure 17. This velocity was chosen to provide easy comparison with the results in Damiano (1998) where all predictions are based on this velocity. However, this velocity is two orders of magnitude greater than the region of 0 to $20\,\mu\mathrm{m\,s^{-1}}$ where the red cell pop out phenomenon is observed in Vink & Duling (1996). For the rigid pellet model employed herein all results for the pressure distribution scale linearly with the velocity and thus it is a simple matter to convert the pressure profiles in figure 17 to velocities characteristic of the pop out regime. In Damiano's model the local rate of change in isotropic membrane tension is in equilibrium with the fluid shear stress and both membrane bending and shear elasticities are neglected. Secomb *et al.* (1986) have shown that this is a good approximation at high red cell velocities. In this limit the red cell assumes a shape that is very close to a circular cylinder with a hemispherical cap. In our rigid pellet model the relative penetration of the red cell membrane into the glycocalyx at the trailing edge is given by $\beta = (r_c(0) - r_c(L))/(R - r_c(L))$. This can be written as $\beta = 1 - 1/k$ in terms of the matrix compression ratio k defined previously. The curves in figure 17 show a large pressure increase over the length of the cell that grows exponentially as the penetration β increases. The behaviour of the pressure resembles that presented earlier for a gliding plane, except for the large pressure drop that occurs across the cell due to the pressure-driven flow. The curves with symbols in figure 17 are the pressure profiles for $\alpha = 0$, a rigid tube without

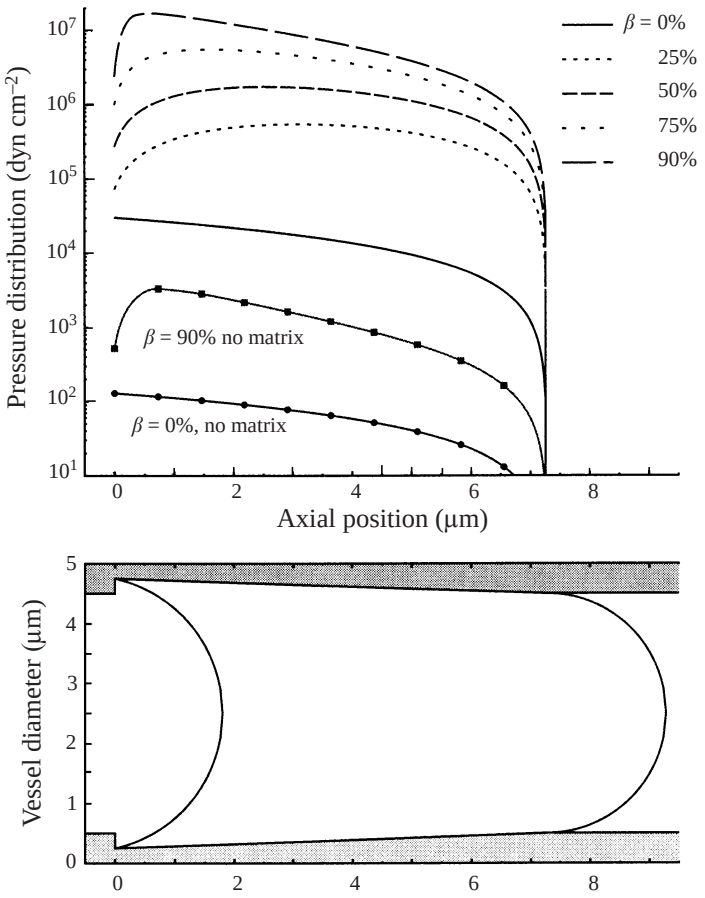

FIGURE 17. Dimensional pressure distribution over the length of a red cell moving at 0.1 cm s^{-1} in a 5 μm diameter vessel with a uniform 0.5 μm thick glycocalyx as a function of the penetration parameter $\beta = 1 - 1/k$. The viscosity of the plasma μ is assumed to be 0.01 dyn s cm^{-2}. Five curves are presented from no penetration, to high penetration. Note the pressure drop increases by almost three orders of magnitude when the membrane invades 90% of the glycocalyx at the trailing edge. The maximum pressure shifts to the trailing edge due to the large resistance of the compressed fibres in that region. For comparison, results for a smooth capillary tube ($\alpha = 0$) with $\beta = 0$, 0.9 and $h_2 = 0.5$ μm are shown by the lower curves with symbols.

glycocalyx, in which the parameter $\beta = 0$ and 0.9. The monotonically increasing profiles for $\beta = 0$ are qualitatively similar to those predicted in Damiano (1998).

The value of α for the undeformed matrix for the curves in figure 17 is approximately 1000 and the pressure differential on the hemispherical caps is the primary contribution to the total driving force. In fact, the zero drag condition applied on the red cell membrane requires that this pressure drop be balanced by the summation of the shear stress and the component of the pressure on the inclined surface in the axial direction. Since there is only a small bulk flow except near the leading and trailing edges where there are steep pressure gradients, one finds (not shown) that the shear stress on the red cell does not vary significantly as the membrane penetrates the glycocalyx, but the pressure contribution grows substantially due to the large increase in drag from the fibres. Physically, the fluid within the matrix has to be expelled by the slanting membrane. Thus, a much greater driving force is needed to achieve

the same cell velocity, compared to the non-penetrating case. The high penetration creates a large pressure drop across the cell, an effect which was absent for the gliding motions of a planar surface over a wall in an unbounded medium considered in § 4. The results in figure 17 provide only a rough qualitative guide to the increase in the pressure drop that results from the glycocalyx penetration at low red cell velocities. The large increase in pressure would deform the cell and at these low velocities the bending moments associated with the membrane skeleton would play an important role in determining the deformed cell shape. The elegant analysis in Secomb *et al.* (1986), which considers these bending moments, is required to determine more realistic red cell shapes. Despite this limitation figure 17 provides a rough description of the pop out phenomenon. The curve for $\beta = 0.9$ would be representative of the initial configuration and as the red cell velocity increased the value of β would decrease, leading to a family of curves similar to that shown in figure 17. In figure 17 the velocity is constant whereas in the pop out the pressure driving force is constant and the velocity of the red cell would increase.

The presence of the glycocalyx affects two important rheological quantities: the apparent viscosity ratio, $\mu_{\rm app}$, and the ratio of tube-to-discharge hematocrit, H_T/H_D. These quantities can be determined from the solution for the driving force $\pi R^2 \Delta P$ over the entire length of the cell and the actual flux through any cross-section.

Because the repulsive force generated within the glycocalyx prevents the cell from touching the capillary wall, the red cells will be driven toward the centre of the capillary. As a result, the red cell velocity U_c is greater than the average plasma velocity, $\bar{u}$. By applying mass conservation, one can readily show that

$$\frac{\bar{u}}{U_c} = q_0 = \frac{H_T}{H_D}. \tag{6.10}$$

Figure 18(a, b) shows the pressure drop ΔP across the length of the cell and the tube-to-discharge hematocrit ratio H_T/H_D for both 5 and 6 μm capillaries lined with a 0.5 μm thick glycocalyx. It is seen that ΔP grows exponentially with respect to the penetration parameter β, whereas H_T/H_D approaches unity. The increase of H_T/H_D agrees with one's intuition, since the effective diameter of the capillary is reduced as the cell penetrates the glycocalyx. For a given value of penetration, the 6 μm capillary always exhibits a larger average flux since the fractional area occupied by the cell is larger than for a 5 μm capillary. However, the pressure drop for a 6 μm capillary is lower than for a 5 μm capillary primarily due to the decreased length of the moving red cell, since cell volume is conserved.

We are particularly interested in examining whether the red cell membrane will penetrate the glycocalyx when the cell moves at velocities $U_c > 100\,\mu{\rm m\,s^{-1}}$. The apparent viscosity ratio of whole blood moving in a capillary is given by Damiano (1998) as

$$\mu_{\rm app} = \frac{1}{8}\left[\frac{R}{L}\frac{{\rm d}p_0'}{{\rm d}z'} + \frac{\pi R^3}{V_c}\left(\Delta p' - \frac{\bar{u}}{U_c}\frac{{\rm d}p_0'}{{\rm d}z'}\right) H_D\right], \tag{6.11}$$

where V_c denotes the cell volume, $\Delta p'$ is the dimensionless pressure drop over the cell, and ${\rm d}p_0'/{\rm d}z'$ is the dimensionless pressure gradient in the plasma between cells; ${\rm d}p_0'/{\rm d}z'$ can be obtained from the solution for a pressure-driven flow in a tube coated by a layer of glycocalyx in the absence of red cells. The prime indicates dimensionless variables. The difference between (6.11) and the original equation (21) in Damiano (1998) arises from the characteristic length in the axial direction. We have used the

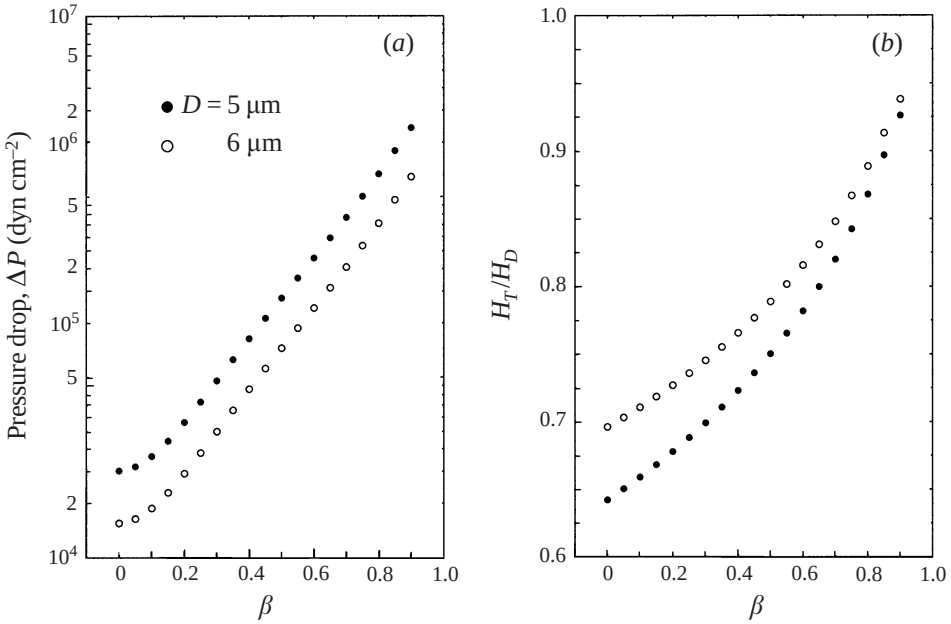

FIGURE 18. (*a*) Dimensional pressure drop over the cell length as a function of penetration parameter $\beta = 1-1/k$ for both 5 and 6 μm capillaries lined with a 0.5 μm thick glycocalyx for a red cell moving at 0.1 cm s^{-1}. (*b*) The ratio of tube-to-discharge hematocrit H_T/H_D for same capillary geometry as in (*a*). Note that for the 6 μm capillary, the effective diameter of the cell is also larger. Both curves approach unity as the penetration increases.

total length of the red cell, L, as the characteristic length scale, whereas Damiano used the radius of the capillary instead.

The apparent viscosity ratio calculated using (6.11), even when $\beta = 0$ in figure 17 and the red cell moves at the edge of the glycocalyx, is one order of magnitude larger than that measured *in vivo* (Pries *et al.* 1994). This suggests that at high velocities a thin fluid layer may exist between the edge of the glycocalyx and the red cell. This hypothesis is consistent with the measurements in Vink & Duling (1996) and Henry & Duling (1999). However, Damiano's calculations, which assume the presence of such a fluid layer, predict values of μ_{app} for 5, 6 and 7 μm capillaries which are a factor of 4 lower than the experimental observations in Pries *et al.* (1994). The large difference in the predicted value of Δp or μ_{app} between Damiano and the results in figure 18(*a*) for $\beta = 0$ is due to two effects. One is the large difference in Darcy resistivity assumed in the two models for the undeformed matrix and the second is the thin plasma layer just mentioned. In our model, the undeformed matrix has a hydraulic resistivity of $O(10^{11})$ dyn s cm^{-4}, corresponding to an open gap between fibres Δ_{2H} of 7 nm. This resistivity is three orders of magnitude greater than that used in Damiano (1998). The values assumed for the Darcy resistivity in Damiano are based on filtration gels with proteoglycans rather than experiments where the capillary selectivity and permeability coefficients are measured *in vivo* as in the present analysis. If we want to match the measured μ_{app}, our calculations indicate that a hydraulic resistivity which is approximately $O(10^{10})$ dyn s cm^{-4} should be used if there is no pure fluid layer above the glycocalyx. If there is a pure fluid layer above the glycocalyx and our predicted resistivity for a fibre spacing of 7 nm is used, we find that the measured μ_{app} of 11 for a 5 μm capillary in Pries *et al.* (1994) can be achieved if the thickness of this pure fluid

layer is about 0.1 μm. This is about 2.5% of the functional diameter of the capillary. However, if Damiano's resistivity is used, one finds that the red cell membrane would need to penetrate 75% of the glycocalyx at the trailing edge in order to match the measured $\mu_{app} \approx 11$. If the red cell were to just fill the entire lumen and not invade the glycocalyx, the calculated μ_{app} using Damiano's resistivity is approximately 5.2. This is still only one half the measured value. While the mechanical properties of the glycocalyx are still open to question, the present model for K_p compares more favourably with the measurements in Vink & Duling (1996) where the edge of the FITC-dextran column is approximately 0.2 μm from the edge of the red cell when it is moving with velocities greater than 125 μm s^{-1}.

Secomb *et al.* (1998) introduced a variable K_p in their model which allows for a transition layer at the outer edge of the glycocalyx. However, their results indicate that varying the thickness of this transition layer over the range 0.05–0.4 μm has very little effect on H_T/H_D and the pressure drop ΔP. In the *in vitro* experimental investigation of Adamson & Clough (1992), where cationized ferritin (CF), 10 nm diameter, was used as a marker for the outer edge of the endothelial surface glycocalyx in frog mesentery capillaries, one observes a uniform layer of about 100 nm separating the capillary wall and the CF layer when plasma is present. The electron micrographs of the vessel wall show that the CF layer forms a sharp and distinct interface at the edge of the surface glycocalyx. Since the glycocalyx is negatively charged, CF would have exhibited a diffuse labelling at the outer edge of the matrix if there were loosely spaced fibres in this region. These results support the hypothesis that the molecular sieve starts at the edge of the glycocalyx and that there is no transition layer of sparser matrix near its edge. The recent experiments of Henry & Duling (1999) lend further credence to this hypothesis. These investigators examined the penetration of the glycocalyx by both low and high molecular weight FITC-dextrans. They observed that FITC-dextran-70 is able to penetrate the outer border of the glycocalyx only after sustained treatment with the enzyme hyaluronidase and that the depth of penetration depended on both the dose and time. In contrast, large (above 500 kDa) FITC-dextrans were still excluded. One would conclude that the smaller structures that determine the molecular sieve (most likely glycoprotein side chains) are selectively removed starting at the outer edge of the glycocalyx, but that in the deeper regions these structures are still present. This suggests that the molecular sieve for the low molecular weight dextrans is distributed throughout the surface matrix layer.

7. Concluding remarks

Motivated by recent *in vivo* studies in the microcirculation and a rapidly growing recognition of the importance of the endothelial glycocalyx, we have developed a generalized lubrication theory for highly compressible porous layers based on an effective-medium approach. This theory also accounts for order of magnitude variations in the Darcy permeability within the porous layer. The predictions of this theory support Vink & Duling's (1996) *in vivo* experimental observations for both the pop out phenomenon and final equilibrium position of the red cell at physiologically observed velocities in 5–7 μm diameter mammalian capillaries. When a 8 μm red cell first squeezes into a capillary of smaller diameter or when it passes through an arterial sphincter, it will elongate and crush the glycocalyx if its velocity is small. As the red cell velocity increases, the red cell membrane will gradually rise off the vessel wall due to the large repulsive force generated within the glycocalyx. This pop out is characterized by an increased clearance between the capillary wall and the red cell membrane. The

measurements in Vink & Duling (1996) indicate that when $U_c > 20\,\mu\mathrm{m\,s^{-1}}$, the cell membrane will first lift off the glycocalyx, creating a thin layer of plasma between the matrix and the red cell membrane whose thickness then increases with increasing U_c. Although the present results are for a rigid planar membrane, the theory can be extended to a deformable red cell membrane using the approach in Secomb *et al.* (1986). Of particular interest is the effect of membrane bending moments on red cell shape at low velocities where there are large compressions of the extracellular matrix. Future work should also include the possible existence of another thin layer of deformable surface glycocalyx coating the red cell membrane, an effect which is not taken into account in the present model.

When the present theory is applied to the motion of a ski or snowboard, a strikingly similar behaviour is observed for the pressure distribution and the lift force. By introducing a small tilt angle, a hydrodynamic lift force can be generated which is large enough to sustain a 70 kg human. Several extensions of the basic problem treated in this paper are of interest. In an effort to understand more sophisticated manoeuvres in skiing, such as turning and stopping, one must consider the mechanics of edging, where the snow powder is compressed in the transverse direction. The numerical method adopted in § 5 is greatly simplified when the lubricating layer does not vary in the transverse direction. This method needs to be generalized to apply to the situation in which h is an arbitrary function of both x and y. The present theory is only qualitatively applicable to long slender planing surfaces, such as skis, where the lubrication approximation $H/W \ll 1$ is not valid. A second complication is that transverse pressure gradients are much larger than the centreline pressure gradients leading to characteristic transverse velocities where inertial effects can be important. For these situations a simplified one-dimensional analysis needs to be developed using a centreline theory that takes into account fluid inertia.

In principle nonlinear inertial effects are not difficult to include. Since the Darcy term appearing in the Brinkman equation can also be incorporated in the Navier–Stokes equation to represent an average effect of the porous material (Hornung 1996), one can investigate the relative importance of viscous dissipation, fluid inertia and matrix deformation in the time-dependent draining of fluid from thin fibre matrix layers, where one has an inertial squeeze film between two closely juxtaposed solid surfaces.

The authors acknowledge the financial support from NIH grant HL 44485. This research was performed by J. Feng in partial fulfillment of the requirement of the PhD degree from the City University of New York.

REFERENCES

Adamson, R. H. & Clough, G. 1992 Plasma proteins modify the endothelial cell glycocalyx of frog mesenteric microvessels. *J. Physiol.* (*Lond.*) **445**, 473–486.

Arons, E. M. & Colbeck, S. C. 1995 Geometry of heat and mass transfer in dry snow – a review of theory and experiments. *Rev. Geophys.* **33**, 463–393.

Barnard, A. C. L., Lopez, L. & Hellums, J. D. 1969 Basic theory of blood flow in capillaries. *Microvasc. Res.* **1**, 23–34.

Brinkman, H. C. 1947 A calculation of the viscous force exerted by a flowing fluid in a dense swarm of particles. *Appl. Sci. Res.* A **1**, 27.

Curry, F. E. 1986 Determinants of capillary permeability: a review of mechanisms based on single capillary studies in the frog. *Circ. Res.* **59**, 367–380.

Damiano, E. R. 1998 The effect of the endothelial-cell glycocalyx on the motion of red blood cells through capillaries. *Microvascular Res.* **55**, 77–81.

Damiano, E. R., Duling, B. R., Ley, K. & Skalak, T. C. 1996 Axisymmetric pressure-driven flow

of rigid pellets through a cylindrical tube lined with a deformable porous wall layer. *J. Fluid Mech.* **314**, 163–189.

Ethier, C. R. 1991 Creeping flow through heterogeneous fibrous materials. *AIChE J.* **37**, 1227–1236.

Feng, J., Ganatos, P. & Weinbaum, S. 1998 Motion of a sphere near planar confining boundaries in a Brinkman medium. *J. Fluid Mech.* **375**, 261–292.

Feng, J. & Weinbaum, S. 2000 A model for flow through a planar orifice in a fibre-filled medium with application to fenestral pores in biological tissues. *Chem. Engng Sci.* (to appear)

Fitz-Gerald, J. M. 1969 Mechanics of red-cell motion through very narrow capillaries. *Proc. R. Soc. Lond.* B **174**, 193–227.

Fu, B. M., Weinbaum, S., Tsay, R. Y. & Curry, F. E. 1994 A junction-orifice-fiber entrance layer model for capillary permeability: Application to frog mesenteric capillaries. *J. Biomech. Engng* **116**, 502–513.

Henry, C. B. & Duling, B. R. 1999 Permeation of the luminal capillary glycocalyx is determined by hyaluronan. *Am. J. Physiol.* **277**, H508–H514.

Hornung, H. 1996 *Homogenization and Porous Media.* Springer.

Hou, J. S., Mow, V. C., Lai, W. M. & Holmes, M. H. 1991 An analysis of the squeeze-film lubrication mechanism for articular cartilage. *J Biomech.* **25**, 247–259.

Howells, I. D. 1974 Drag due to the motion of a Newtonian fluid through a sparse random array of small fixed rigid objects. *J. Fluid Mech.* **64**, 449–475.

Howells, I. D. 1998 Drag on fixed beds of fibres in slow flow. *J. Fluid Mech.* **355**, 163–192.

Hu, X. & Weinbaum, S. 1999 A new view of Starling's hypothesis at the microstructural level. *Microvascular Res.* **58**, 281–304.

Jordan, R. E., Hardy, J. P., Perron, F. E. & Fisk, D. J. 1999 Air permeability and capillary rise as measures of the pore structure of snow: an experimental and theoretical study. *Hydrological Proc.* **13**, 1733–1753.

Kenyon, D. E. 1979 A mathematical model of water flux through aortic tissue. *Bull. Math. Biol.* **41**, 79–90.

Lai, W. M. & Mow, V. C. 1980 Drag-induced compression of articular cartilage during a permeation experiment. *Biorheology* **17**, 111–123.

Lighthill, M. J. 1968 Pressure-forcing of tightly fitting pellets along fluid-filled tubes. *J. Fluid Mech.* **34**, 113–143.

Luft, J. H. 1965 Fine structure of capillary and endocapillary layer as revealed by ruthenium red. *Proc. Fed. Am. Soc. Expl Biol.* **25**, 1773–1783.

Lundgren, T. S. 1972 Slow flow through stationary random beds and suspensions of spheres. *J. Fluid Mech.* **51**, 273–299.

Michel, C. C. 1997 Starling: the formation of his hypothesis of microvascular fluid exchange and its significance after 100 years. *Expl Physiol.* **82**, 1–30.

Orszag, S. A. 1971 Accurate solution of the Orr–Sommerfeld stability equation. *J. Fluid Mech.* **50**, 689–703

Pries, A. R., Neuhaus, D. & Gaehtgens, P. 1992 Blood viscosity in tube flow: Dependence on diameter. *Am. J. Physiol.* **263**, H1770–H1778.

Pries, A. R., Secomb, T. W., Gessner, T., Sperandio, M. B., Gross, J. F. & Gaehtgens, P. 1994 Resistance to blood flow in microvessels in vivo. *Circ. Res.* **75**, 904–915.

Sangani, A. S. & Acrivos, A. 1982 Slow flow past periodic arrays of cylinders with application to heat transfer. *Intl J. Multiphase Flow* **8**, 193–206.

Schlichting, H. 1979 *Boundary Layer Theory*, 6th Edn. McGraw-Hill.

Schmid-Schoenbein, H. 1999 Self organized blood flow observed by in *in vivo* rheoscopy: High resolution flow visualization of red blood cells traveling from the arterioles to the vessels in living microvascular beds. *Plenary Lecture Euromech. Colloquium* 389, *Gratz, Austria, April* 20–24.

Secomb, T. W. & Gross, J. F. 1983 Flow of red blood cells in narrow capillaries: role of membrane tension. *Intl J. Microcir. Clin. Exp.* **2**, 229–240.

Secomb, T. W., Hsu, R. & Pries, A. R. 1998 A model for red blood cell motion in glycocalyx-lined capillaries. *Am. J. Physiol.* **274**, Heart Circ. Physiol. 43:H1016–1022.

Secomb, T. W., Skalak, R., Ozkaya, N. & Gross, J. F. 1986 Flow of axisymmetric red cell in narrow capillaries. *J. Fluid Mech.* **163**, 405–423.

Tam, C. K. W. 1969 The drag on a cloud of spherical particles in low Reynolds number flow. *J. Fluid Mech.* **38**, 537–546.

Tozeren, H. & Skalak, R. 1978 The steady flow of closely fitting incompressible elastic spheres in a tube. *J. Fluid Mech.* **87**, 1–16.

Tsay, R. & Weinbaum, S. 1991 Viscous flow in a channel with periodic cross-bridging fibres: exact solutions and Brinkman approximation. *J. Fluid Mech.* **226**, 125–148.

Vink, H. & Duling, B. R. 1996 Identification of distinct luminal domains for macromolecules, erythrocytes and leukocytes within mammalian capillaries. *Circ. Res.* **71**, 581–589.

Wang, H. & Skalak, R. 1969 Viscous flow in a cylindrical tube containing a line of spherical particles. *J. Fluid Mech.* **38**, 75–96.

Wang, W. & Parker, K. H. 1995 The effect of deformable porous surface layers on the motion of a sphere in a narrow cylindrical tube. *J. Fluid Mech.* **283**, 287–305.

Weinbaum, S. 1998 Models to solve mysteries in biomechanics ar the cellular levels; a new view of fibre matrix layer. *Ann. Biomed. Engng.* **26**, 1–17.

Weinbaum, S., Tsay, R. & Curry, R. E. 1992 A three-dimensional junction-pore-matrix model for capillary permeability. *Microvascular Res.* **44**, 85–111.